INNOVATIVE CLEAN COAL TECHNOLOGY (ICCT)

180 MW DEMONSTRATION OF ADVANCED TANGENTIALLY-FIRED COMBUSTION TECHNIQUES FOR THE REDUCTION OF NITROGEN OXIDE (NOx) EMISSIONS FROM COAL-FIRED BOILERS

ESP Performance Analysis

DOE Contract Number
DE-FC22-90PC89653

SCS Contract Number
C-91-000028

Prepared by:

Southern Research Institute
for
Southern Company Services, Inc.
800 Shades Creek Parkway
Birmingham, Alabama 35209

Cleared by DOE Patent Counsel in October 1993

ESP PERFORMANCE ANALYSIS DURING THE 180 MW DEMONSTRATION OF ADVANCED TANGENTIALLY-FIRED COMBUSTION TECHNIQUES FOR THE REDUCTION OF NITROGEN OXIDE EMISSIONS FROM COAL FIRED BOILERS

Prepared by

E. C. Landham, Jr.
M. G. Faulkner

SOUTHERN RESEARCH INSTITUTE
2000 Ninth Avenue South
P. O. Box 55305
Birmingham, AL 35255

Prepared for

SOUTHERN COMPANY SERVICES
P. O. Box 2625
Birmingham, AL 35202

SCS Contract 196-90-107

Rob Hardman
Project Manager

September 1993

SRI-ENV-93-824-7215-v

CONTENTS

1. INTRODUCTION

Southern Company Services and the U.S. Department of Energy have conducted a demonstration of advanced combustion techniques for reduction of NO_x emissions on the 180 MWe tangentially-fired, pulverized-coal boiler at Plant Lansing Smith, Unit 2, of Gulf Power Company. Southern Research Institute, a subcontractor on this program, was responsible for evaluation of the effects of the NO_x reduction techniques on the particulate control system (electrostatic precipitator). This report presents the particulate control results of the demonstration program which was conducted under SCS contract number 196-90-107.

The demonstration program consisted of four test conditions which evaluated the effects of four major variations of the combustion conditions. The four conditions included were:

1. Baseline (No Low-NO_x modifications)
2. Low-NO_x Concentric-Firing-System Level 1 (LNCFS 1)
3. Low-NO_x Concentric-Firing-System Level 2 (LNCFS 2)
4. Low-NO_x Concentric-Firing-System Level 3 (LNCFS 3)

The exact descriptions of the furnace setup and combustion conditions are contained in reports from other contractors on this project. During each of the programs, the characteristics of the boiler effluent which would be expected to affect an electrostatic precipitator (ESP) were measured under three load conditions:

1. 180 MW (Full-Load)
2. 135 MW
3. 115 MW

Measurements were also made during the three LNCFS test programs at the Unit's maximum output of 200 MW, but no baseline data were collected at this load for comparison. Measurements made at the inlet to the hot-side ESP on Unit 2 during each test condition include: particle mass loading, gas volume flow, gas temperature, and particle size distribution of the fly ash. Vapor-phase SO_2 and SO_3 concentrations were measured at the inlet to the cold-side ESP. In addition, the electrical conditions of the ESP were measured for correlation with particle size and resistivity measurements.

In support of the field effort, laboratory measurements of chemical composition, loss-on-ignition, carbon content, and electrical resistivity were made on fly ash samples collected during the test program. Estimates of fly ash resistivity based on coal and ash composition were also made using a computer resistivity model.

A computer model of ESP performance was used to assess the effects that low-NO_x modifications would have on ESP operation. The changes attributable to LNCFS were used in the model to generate performance comparisons that would show the expected ESP performance differences between the different LNCFS levels. The modeling was performed for a series of hypothetical ESPs using both the hot-side conditions measured at Lansing Smith and estimated cold-side conditions.

Section 2 of this report compares and discusses the field and lab measurement data. ESP modeling results illustrating the theoretical effects of the LNCFS modifications on ESP performance are presented in Section 3. A summary of the significant findings from the program is contained in Section 4.

2. TEST RESULTS

PARTICLE MASS LOADING, GAS FLOW, AND TEMPERATURE

The effects of the changes in combustion conditions on the particle mass and flue gas exiting the furnace were evaluated utilizing EPA Method 17. The Method 17 mass train measurements were made at the inlet of the hot-side ESP (economizer outlet). The results are shown for the four LNCFS conditions and four boiler loads in Table 1. Three sets of data are shown for the 180 MW LNCFS 3 tests. The first entry was the initial LNCFS 3 test, which was conducted with considerable wear on the coal mills. The second LNCFS 3 also test was conducted with the worn mills but with the coal mill classifier settings adjusted to produce a finer coal size distribution. The last LNCFS 3 test was performed during a later test phase after the coal mills had been overhauled. Similarly, the 135 MW data contain two LNCFS 3 tests, which were performed before and after the mill overhaul. Since no baseline test data were taken on the 200 MW load condition, only entries for LNCFS Levels 1 - 3 are shown for this load.

The flue gas oxygen content measured during each of the test programs is shown in the rightmost column of Table 1. The flue gas oxygen content is a direct indication of the amount of excess air used for combustion. In the absence of other changes, increased excess air will result in an increase in flue gas volume and velocity and a decrease in particle mass loading. The increased flow will cause a decrease in the effective size of the ESP and therefore decrease its collection efficiency. Considerable variation is observed in the oxygen data measured by Method 17, with values which range from 3.5% to 5.6%. In addition, the values are inconsistent even within an LNCFS condition.

Table 2 compares the full-load flue-gas oxygen content for the different test phases measured by other contractors using continuous monitors during long-term tests [1]. The data taken by SRI (Table 1) are short-term measurements that were made during the mass train runs at the beginning of the test period of each LNCFS level. The long-term measurements should be more representative of typical operation for each LNCFS condition. The oxygen differences shown in Table 2 are assumed to be an actual difference between the LNCFS levels. For this reason, the long-term oxygen measurements will be used for ESP modeling and analysis. The effect of these

differences in oxygen and gas flow on ESP performance will be assessed a subsequent section on ESP modeling. Because of the inconsistency in the oxygen values between the short- and long-term data, the gas volume flow values in Table 1 are not valid for comparison.

The particle mass loadings are presented in Table 1 as gr/acf (actual measured loading), gr/dscf (normalized for temperature, pressure, and moisture, and lb/10^6-Btu (further corrected to 0% oxygen). Comparison of the mass loadings for various test programs on a actual basis is not appropriate since significant differences were observed in flue gas moisture, which is a property of the coal and should not be affected by the combustion modifications. Similarly, comparison of values normalized with either no oxygen in the flue gas or with inappropriate oxygen levels do not represent the effects of excess air for dilution of the mass loading. The most appropriate comparison is to normalize the measured gr/dscf values to the oxygen values observed during the long-term tests (Table 2). This should represent the mass values which would result under the long-term conditions. The adjusted mass values are shown in Table 3.

Figure 1 plots the adjusted mass loadings as a function of boiler load. The data points are scattered between 2.5 and 3.5 gr/dscf with no clear trend in the values. At low load, the LNCFS 1 and 3 data were consistently higher than the baseline data, but at full-load (180 MW) the difference was insignificant. The LNCFS 2 data did not indicate higher mass at the lower loads. Interestingly, the overhaul of the coal mills generally produced a greater effect on full-load mass loading than did the change in LNCFS conditions (comparison of inverted triangles vs squares). Therefore, we conclude that low-NO_x operation did not produce a significant and consistent effect on the particle mass entering the ESP during full-load operation.

The dotted lines on Figure 1 show the range of typical ESP inlet mass loadings calculated from the EPRI database [2] based on the ash content of the coal (Table 4). The dotted lines actually represent the upper and lower 50% confidence intervals to the database mass distribution. Except for the 135 MW LNCFS 1 data point, which appears to be an outlier in any case, the Lansing Smith mass data all fall within the top half of the range considered typical of this coal and furnace type.

The average flue gas temperatures for each test condition are shown in Table 1 and are plotted as a function of boiler load in Figure 2. At the lowest loads, the LNCFS 1 and 2 conditions indicate the highest temperatures. This could be a result of the low-NO_x modifications, but could also be affected by ambient temperatures which were 35°F higher during these two tests. All of the temperatures converge at 180 MW except for the LNCFS 2 data, which remain approximately 10°F higher than the other conditions. However, considering the measurement range, we consider this to be in the noise range for this measurement. In any case, a 10°F difference at 670°F will not affect the operation of the ESP and can be disregarded.

FLY ASH PARTICLE SIZE DISTRIBUTION

The measured size distributions of the fly ashes collected at the ESP inlet for all the test programs are compared in Figures 3 through 11. The nine figures are divided into three groups which represent the results for the three boiler loads tested: 180, 135, and 115 MW. No measurements of size distribution were made during any 200 MW tests or the LNCFS 3 retests. Within each group, cumulative mass loading as a function of size is shown in the first figure. Each data point on this graph represents the mass concentration (mg/acm) contained in all particles smaller than the diameter at which the point is plotted. The second figure of each group shows the particle size distribution data on the basis of percent of the total mass smaller than the indicated size. The derivative of the inlet cumulative mass size distribution for the three load conditions is shown in the third figure of the group. This method of presenting the data illustrates the particle sizes where mass is concentrated and helps to highlight differences between distributions. In any size interval, the area under the differential curve represents the amount of mass contained in that interval. The error bars on the graphs represent 90% confidence intervals to the average distributions.

The size distributions measured for normal full-load (180 MW) operation (Figures 3 - 5) indicate no measurable differences for particles smaller than 5 μm. This is important, since the smaller particles affect ESP performance and opacity much more than do larger particles. At full load, the distributions do indicate differences in the concentrations of large particles. The differences shown among the conditions are much greater than those measured with the Method 17 mass trains (Table 1 or 3). However, cascade impactors do not provide a particularly accurate

measure of total mass loading because isokinetic nozzle velocities are not maintained at every sample point. Thus the data in Table 3 should be used for total mass loadings, while the impactor data are used for the smaller particles.

At 135 MW (Figures 6 - 8) and 115 MW (Figures 9 - 11), good agreement for the various conditions is observed for large particles. Once again this disagrees with the mass trains which, in these cases, did indicate differences in total mass. The total mass loading at the ESP inlet is primarily controlled by large particles. Therefore, the same caution concerning anisokinetic errors applies to these data, but it is surprising that better agreement is not seen between the two measurement systems. Minor differences are seen in the submicron size range for the lower loads, but the differences are generally small and inconsistent.

The shaded, bounded areas on the graphs in Figures 3, 6, and 9 indicate the cumulative mass distribution (± 50% confidence intervals) predicted by the EPRI database for a typical bituminous coal burned in a pulverized-coal-fired boiler, using the average ash content of the coal (8.8%). Although some of the data lie outside the predicted range, the general trend of the data is in good agreement with the predictions. This indicates that the distribution of fly ash particles produced by the LNCFS low-NO_x modifications was typical of that expected when burning a bituminous coal.

The mass-mean-diameter (mmd), which is the particle size corresponding to 50% on Figures 4, 7, and 10, is about 18 μm for all data sets. Assuming a log-normal distribution, a geometric standard deviation (σ) of about 3.4 can then be computed. The EPRI database predicts an mmd of 16.3 μm and a σ of 3.4 for bituminous coal, again implying that the measured size distributions for the LNCFS tests were typical of a bituminous coal.

FLY ASH CHEMICAL COMPOSITION

The electrical resistivity of fly ash, which strongly affects ESP performance, is highly dependent on the chemical composition of the ash [3]. In order to examine the chemical nature of the fly ash from the test phases, samples were collected from the ESP inlet and middle field hoppers (both North and South sides) during each test day. Specimens collected on the days that total

mass measurements were made were selected for analysis. Portions of samples from the inlet and middle field hoppers were blended proportionately to approximate the composition of the fly ash at the ESP inlet. The proportions were determined by using the estimated overall efficiency of the ESP and assuming each field had constant collection efficiency. Although some dust particles escape the ESP, these particles account for only a very small percentage of the total mass and should not seriously impair the representative nature of the blended samples.

The average chemical compositions of the hopper samples from the various phases are compared in Table 5. Some variations in the chemical compounds known to affect resistivity (principally Li_2O, Na_2O, MgO, CaO, and Fe_2O_3) are evident. Although most changes in the ash chemistry would be due to changes in the coal supply and not because of changes in combustion conditions, some effects of LNCFS are possible. Sodium is an element which is critical to proper operation of hot-side ESPs and can also have significant effects on ash resistivity at cold-side temperatures. Since at least part of the sodium in the coal is volatilized at flame temperatures and subsequently condensed on particles and furnace surfaces, combustion changes could affect the sodium content of the fly ash exiting the furnace and thus affect the resistivity. Figure 12 plots ash sodium content as a function of boiler load for all of the major test conditions. Although some differences can be seen, they are not large enough to produce substantial effects on resistivity. In addition, to correctly attribute the change in ash sodium to the combustion conditions, comparison of the fly ash, bottom ash, and coal ash sodium contents would be required. However, since the changes observed are so slight, this step was not taken.

The carbon content of the fly ash was determined for the isokinetically-collected mass train samples. The results of these measurements are shown in Table 6 for the total sample and for size-segregated fractions of each sample. Also shown are the loss-on-ignition (LOI) values obtained from analysis of both the mass train and the ESP hopper samples. As can be seen from the table, most of the LOI in the mass train samples is associated with the large particle fraction (greater than 200 mesh). It is also evident from Table 6 that essentially all of the LOI is carbon. The LOI associated with the ESP hopper samples is higher than the mass train samples in all cases, and is up to 2.5% higher for some samples. The reason for the discrepancy may be related to the time averaging characteristics of the ESP. That is, high-carbon ash collected

in the ESP during load rise and other transient periods may affect the hopper ash composition even hours later under stable operating conditions.

Figure 13 shows the relationship between boiler load and fly ash carbon content for each of the test phases. The only clear dependency of carbon on load occurs from 180 to 200 MW where carbon always increased. The original LNCFS 3 data indicated higher carbon for low loads, but came close to the baseline value at full load (180 MW). Both of the LNCFS 3 retests had much higher carbon carryover.

Also shown on the figure is a single data point obtained during a 180 MW baseline test with low excess air in the furnace. This condition produced the highest ash carbon value observed during the entire program. Comparison with the LNCFS carbon data provides additional perspective on the magnitude of the LNCFS effects.

Values of LOI which are greater than 5 to 8% can result in ESP particle emissions problems. The detrimental effects are thought to be a result of preferential reentrainment of the very low resistivity carbon particles. Many of the samples from the LNCFS tests have values in the 5-8% range where an effect could occur. However, the relationships between LOI values, the form and size of carbon particles, and ESP performance are not well defined. Therefore, we cannot conclusively determine if the fly ash carbon contents measured would affect ESP performance.

FLUE GAS COMPOSITION

Most of the measurements to quantify the effects of LNCFS were made at the inlet of the hot-side ESP on Unit 2. However, the majority of existing ESP installations operate at cold-side temperatures, so any gas parameters that would affect operation of a precipitator at these lower temperatures must also be considered. One very important consideration is the presence of sulfuric acid vapor (generally referred to as SO_3) in the flue gas. The vapor-phase concentration of SO_3 which exists at equilibrium with the fly ash particles can substantially affect the electrical resistivity of the fly ash due to acid adsorption on the particle surfaces at temperatures below 400°F. At higher temperatures common to hot-side operation, the resistivity of the ash is unaffected by the presence of the acid vapor. Further, plants with regenerative air heaters

commonly experience loss of 50% or more of the SO_3 vapor across the air heater. This loss occurs through the adsorption of acid on the fly ash particles and through condensation of the acid on cool air-heater surfaces. Because of its importance only to cold-side installations, the concentrations of SO_x in the flue gas were measured at the inlet to the cold-side ESP.

Because of the upstream hot-side precipitator, the concentration of particles at the inlet to the cold-side ESP at Lansing Smith will be less than if the cold-side precipitator were the only particle collection device. This will result in fewer particles for the acid vapor to adsorb on, so the values of SO_3 measured at Lansing Smith may be higher than would occur at another installation which uses a cold-side precipitator only. However, the ratio of SO_3 to SO_2 can be compared to that of the other tests under the same load conditions to determine if the LNCFS modifications affect this conversion process.

The measured values of SO_x for the four test phases are compared in Table 7. Since the effect on resistivity is dependent on the actual concentration of SO_3 at duct conditions, the results are not normalized to a common oxygen level. Although there is some variation, the values of SO_2 for each load condition are comparable, with no clear dependence on test phase. There is considerable variation in the SO_3 values which show a fairly clear dependency on boiler load and gas temperature. The lower gas temperatures corresponding to lower boiler loads would be expected to reduce vapor-phase SO_3 concentrations because of greater adsorption of the SO_3 on fly ash particles and other surfaces. An obvious dependency on test condition is not clear from the table, although there are variations which are not explained by load and temperature.

Also shown in Table 7 is the apparent SO_2-to-SO_3 conversion rate, which is simply the ratio of SO_3 to SO_2 converted to a percentage. This ratio accounts for changes in SO_3 which are due to variations in SO_2. The ratio of SO_3 to SO_2 is plotted for the 180 and 135 MW data in Figure 14 as a function of the carbon content in the isokinetically collected fly ash samples (Table 6). Also shown on the graph is an additional data point collected during a low-O_2 condition which was obtained during the baseline test. For these loads, there appears to be a clear trend relating SO_3 and carbon in the ash which transcends the furnace configuration. For some unknown reason, the 180 MW baseline data do not fit the trend well, particularly for the low-O_2 test. When the 180 MW baseline data are excluded, the linear regressions indicated by the lines on the

figure are obtained. The regressions have coefficients of correlation above 0.98 for the both sets of data. The difference in the 180 and 135 MW trends is probably the result of lower gas temperature at the lower load.

Merryman and Levy [4] maintained that the increased local CO values in the furnace during staged combustion could result in increased SO_3 formation, but that this was a transient effect which was not persistent beyond the furnace. An increase in oxidation of SO_2 to SO_3 downstream of the furnace because of the catalytic action of carbon particles is a distinct possibility [5], and may be responsible for the results shown here. Iron in the ash can also catalyze SO_2 oxidation and can often be related to changes in SO_3, but the ash compositions in Table 5 do not indicate appropriate changes in this ash component. However, the disagreement of the 180 MW baseline data indicate that, if the effect exists, it must be related to the form and size of carbon particles or some other unmeasured parameter.

The SO_3 data collected during the 200 MW and 115 MW tests also generally fit the trends shown in Figure 14, but increase the scatter and were not included to simplify the figure. The 115 MW data must be used with caution because large areas of the duct were at or below the acid dewpoint temperature during those tests. At low load, the amount of SO_3 measured may have been reduced by acid lost through condensation.

FLY ASH RESISTIVITY

The electrical resistivity of the fly ash layer collected on the ESP plates is one of the most important factors affecting collection performance of an ESP. High dust layer resistance to the inter-electrode corona current produces a high electric field in the dust layer. When the magnitude of the field in the layer exceeds the breakdown strength of the flue gas, a reverse-discharge phenomenon occurs which limits useful power input to the ESP through premature sparking or back corona. The reduced ESP voltages and currents associated with dust layer breakdown have an adverse effect on collection efficiency. Resistivity values greater than $2x10^{10}$ ohm-cm are generally assumed to affect performance, with increasing effect at higher values.

The preferred method of resistivity measurement is conducted in situ with a point-plane resistivity probe. Unfortunately, this device is not suitable for use at hot-side temperatures or with the low mass loading which exists at the cold-side ESP inlet at Lansing Smith. In order to interpret the effects of the NO_x reduction strategies on the performance of the precipitator and to extrapolate the results of this study to the majority of cold-side ESP installations, some measure of the fly ash resistivity must be obtained. Therefore, this program utilized laboratory resistivity measurements in simulated flue gas environments and resistivity model predictions based on ESP hopper samples in place of in situ measurements.

Hot-Side Temperatures

Data from laboratory resistivity measurements were made on proportionally blended hopper samples from each of the four test phases and at each load. The resistivity curves were acquired in air containing a water vapor level approximately equal to that measured during the tests, using the descending temperature technique. Data from both sides of the ESP (North and South) for each test condition were collected. Graphs of these resistivity curves are presented in Figures 15 - 22.

Values obtained from the resistivity curves are summarized for the operating temperatures of the Lansing Smith ESP in the column labeled "Laboratory Measurement" in Table 8. As expected, changes in gas temperature associated with the various loads produced differences in the

laboratory measured resistivities for different test conditions. These resistivity changes are directly related to the reductions in flue gas temperature at the lower boiler loads. However, all of the values obtained are sufficiently low that ESP performance should not be affected.

The chemical compositions of the ESP hopper samples (Table 5) were used as input to a computer model for predicting resistivity [3]. The results are summarized for hot-side temperatures in the inherent resistivity prediction column of Table 8. The agreement between the laboratory resistivity measurements and the predicted resistivity values is quite good. Both sets of resistivity data concur that the inherent resistivities of these fly ashes should not limit ESP performance at hot-side temperatures.

Hot-side precipitators can experience a deterioration in performance over time (weeks to months) because of a gradual depletion of charge-carrying sodium ions in a thin layer of ash next to the collection plates [6]. The depletion of charge carriers results in an effective resistivity of the dust layer which is significantly higher than the inherent value obtained by the laboratory measurements. Sodium depletion effects have been previously documented at Lansing Smith with a different coal supply [7]. Bickelhaupt developed a method for predicting the increase in resistivity of the ash in a hot-side ESP due to sodium depletion [8]. Using the chemical compositions in Table 5, the increases in resistivity expected because of sodium depletion in the Lansing Smith samples were calculated and are summarized in the last column of Table 8. In general, the resistivity of the sodium-depleted ash layer is predicted to be 1/2 to 1 order of magnitude higher than that without sodium depletion. At the lower loads, the projected resistivity values with sodium depletion (up to $4x10^{10}$ ohm-cm) may be high enough to slightly degrade the performance of the ESP.

Comparing all three methods of determining resistivity we would conclude that no significant effect of LNCFS on resistivity was observed for hot-side conditions. Within a given boiler load, the difference between the baseline and the LNCFS conditions is generally within a factor of two. Where higher differences are observed for one method of determination, the other two methods do not concur. Resistivity values that are within a factor of 2 are normally considered to be in excellent agreement, with little effective difference in ESP performance being observed with less than a half-order-of-magnitude difference. Therefore, it can be concluded that there was no

significant difference in fly ash resistivity for any of these tests and that the low NO_x boiler modifications did not appear to affect the resistivity of the fly ash produced.

Cold-Side Temperatures

The resistivity data shown in Figures 15 - 22 indicate that, at cold-side temperatures (near 300°F), the resistivity of the Lansing Smith fly ash with no SO_3 present would be moderately high (2-6x10^{11} ohm-cm) and would significantly limit ESP performance. However, free SO_3 vapor was found in the flue gas during all of the test phases. The data obtained with acid added to the environment (the data symbols lying below the curves in the figures and tabulated in Table 9) indicate that 4.5 ppm of SO_3 in the flue gas should reduce the resistivity in a cold-side ESP to less than 2x10^9 ohm-cm. This concentration of SO_3 is less than the lowest values measured during the test (Table 7). Since increasing the amount of SO_3 present at cold-side temperatures tends to decrease the measured resistivity, the laboratory resistivity values obtained with 4.5 ppm SO_3 should be the highest that would be encountered by an ESP under these conditions. The resistivities are all sufficiently low that electrical operating conditions of the ESP should not be affected.

Because the laboratory measurement of resistivity with acid vapor is run for an extended period of time in order to reach an equilibrium condition, the resulting values of resistivity with some ashes can be lower than could realistically be achieved at a power plant. This over-conditioning effect does not appear to be related to ash compositions similar to that at Lansing Smith, but the lack of a developed correlation for the effect suggests caution in the interpretation of the laboratory data for cold-side temperatures. However, even if the laboratory resistivity data were as much as an order of magnitude too low, the actual resistivity at Plant Smith would still be low enough not to impede ESP operation.

Resistivity predictions were made using both the measured value of SO_3 and with a constant value of 4 ppm for comparison between phases. The two sets of results are summarized for the typical cold-side temperature of 300°F in Table 9. Some minor variations are observed in the predictions with measured SO_3, but with a constant value of SO_3 no significant differences are evident. There was a dependence of vapor-phase SO_3 concentration on the carbon content of

the fly ash established in a previous section. Since the carbon in the ash was generally related to the combustion conditions, there could be an effect of LNCFS on SO_3 generation. However, since the correlation did not appear to extend to the baseline conditions and varied even within an LNCFS condition, prediction of a precise effect of LNCFS on resistivity because of this effect is not appropriate. In sum, all of the techniques agree that no significant effect on cold-side resistivity should result from LNCFS.

ESP ELECTRICAL CONDITIONS

The electrical operating conditions of the Lansing Smith hot-side ESP were measured for each test condition. The measurements were made using calibrated SRI voltage dividers installed on the high voltage bus of the ESP fields. The results are plotted as average areal current density at the collecting plate versus average voltage for the four 180 MW tests in Figures 23 through 25. Field A is the inlet field, Field E is the third field, and Field J is the fourth field in this five-field deep precipitator. The physical configuration of the electrical fields of the ESP is shown in Figure 26.

Severe back corona would be indicated by regions of infinite or negative slope in the graph of current density versus voltage (commonly referred to as a "V-I curve"). Although not well defined, some evidence of back corona in Fields E and J can be observed in all of the curves. However, although the V-I curves do contain areas where they have infinite or negative slope, these areas are limited and the curves generally maintain a positively-sloped curve, indicating that the back corona is not particularly severe. The electrical operating conditions of the ESP are degraded in all cases, indicating that the sodium depletion resistivity data are most appropriate for understanding the operation of this ESP. The baseline condition exhibits the poorest V-I curves, but this is likely related to the time on-line for sodium depletion to occur. Since sodium depletion is highly time dependent and all of the LNCFS tests occurred a short time after furnace modification and startup, comparison of the electrical conditions is probably not meaningful. Therefore, we would have to conclude that no obvious effects of LNCFS on ESP electrical operation can be discerned under the circumstances.

3. ESP PERFORMANCE MODELING

The low-NO_x modifications to the Lansing Smith boiler produced some changes in the gas and particle effluents which would affect ESP performance. Revision 3 of the EPA/SRI mathematical model of electrostatic precipitation [9] was used to compute the theoretical effects of those changes on ESP performance. This model performs a detailed mathematical simulation of the precipitation process along one gas passage of a wire-plate ESP. The accuracy of the model has been validated by detailed comparison to field data from 18 full-scale ESPs [2].

The ESP installed on Lansing Smith is located on the hot side of the air heater and generally operates at temperatures above 600°F. However, most existing and future ESPs operate on the cold side of the air heater at temperatures around 300°F. The performance of the two types of ESPs can be quite different because of changes in corona generation, operating voltage, gas density, gas viscosity, particle loadings, and particle reentrainment. For this reason, model comparisons of the test conditions were performed for both cold-side and hot-side ESPs.

The modeling was conducted for a series of three hypothetical ESPs of varying sizes which should be representative of the population of existing ESPs. The three ESPs have nominal specific collection areas (SCAs) of 150, 310, and 500 ft^2/1000 acfm under full-load conditions, and correspond to using 3, 5, and 8 collecting fields in the direction of gas flow. The physical specifications of the hypothetical ESPs and a summary of other data used for input to the ESP model are shown in Table 10.

The ESP model has two empirical parameters which account for non-ideal conditions in the ESP. These parameters describe the performance degrading effects of flue gas sneakage and reentrainment (s) and non-uniform gas flow distributions (σ_g). Sneakage is the fraction of dirty gas which avoids each electrified ESP section by passing through hoppers, above plates, etc., while reentrainment is the fraction of collected particles which are subsequently resuspended in the gas stream during electrode rapping and other disturbances. The σ_g parameter is the normalized standard deviation of the gas velocity distribution in the interelectrode space. Values of 0.05 for s and 0.15 for σ_g have been established as generally describing operation of modern ESPs in good condition, while values of s = 0.10 and σ_g = 0.25 provide best agreement for older

ESPs [2]. Both sets of conditions were used in the modeling work to establish an expected range of operation.

The ESP electrical operating conditions used in the model for the series of hypothetical ESPs were obtained from the cold-side operating point correlation in the EPRI data base [2]. The correlation relates the dust resistivity and ESP plate spacing to average ESP electrical operating conditions. Since no significant differences in resistivity could be directly attributed to the low-NO_x modifications, the same electrical conditions were used in baseline and low-NO_x calculations. For cold-side ESPs, a resistivity value of $4x10^{10}$ ohm-cm was used to estimate the electrical conditions, which are shown by field in Table 11. Although this resistivity is higher than the average values obtained during this demonstration, the actual value used in the model is not particularly important to this analysis, since all runs used the same values. This higher resistivity value had to be used because the very low actual resistivity values at Lansing Smith caused the predicted efficiency of the largest hypothetical ESP to exceed the output resolution of the ESP model. A typical value for the hot-side conditions of $2x10^{9}$ ohm-cm was used for those electrical predictions. For cold-side modeling, the predicted electrical conditions were used without modification. However, corona generation occurs more readily at high temperatures resulting in significantly lower voltages for a given current on hot-side ESPs [10]. For the hot-side cases, the predicted current density was used without modification, while the predicted voltage was reduced by the ratio of the gas density for the two temperatures. The corrected hot-side operating conditions are also shown in Table 11.

Since no significant difference was observed in the particle size distributions, the cumulative percent mass particle size distribution measured during the 180 MW baseline test was used in all the model runs after a minor adjustment. The total mass loading indicated by the impactors was slightly lower than that determined by the mass train measurements. Since mass trains are a better indication of total loading, the measured size distribution was adjusted to produce agreement. The disagreement was assumed to be due to isokinetic errors with the impactors, and all of the adjustment was made in particle sizes above 8 μm (the cut point of the first stage).

Although most of the electrical, gas and particle conditions measured during each phase of the LNCFS testing were essentially the same as the baseline test, one factor that did apparently

change between the LNCFS configurations is the excess air contribution to the flue gas volume. Long-term operation data in Table 2 showed that, relative to the baseline test, LNCFS 2 produced a 22% increase in flue gas oxygen, while the LNCFS 3 data indicates a 16% increase. A 13% decrease in flue gas oxygen was measured in the LNCFS 1 test. In the absence of other changes, these differences in flue gas oxygen will produce changes in the gas volume flow and particle mass loading to the ESP and alter its performance.

To estimate the effects of the gas volume changes on ESP performance, the ESP model was run with gas volume, velocity, and dust load changed in proportion to the change in oxygen levels. The remainder of the model inputs were left set to their baseline values. Table 12 shows how the model input parameters were varied for each model condition. The results of the hot-side model calculations are shown in Table 13. Figure 27 illustrates the effect of the low-NO_x modifications by showing the percent change in ESP penetration relative to the baseline test using the better non-ideal conditions. The worst case occurred for LNCFS 2, in which the model predicts an ESP penetration increase of 8% for a small ESP to 27% for a large ESP. For the LNCFS 1 tests, the modeled emissions are less than the baseline case because of reduced oxygen and gas flow. The greater effect for larger ESPs is due to the compounding effects of changed collection efficiency for more ESP fields.

Because of the decreased gas viscosity, decreased particle reentrainment, and increased collecting electric field (voltage) at cold-side temperatures, the model projected the cold-side ESP performance to be better for the same SCA than the hot-side performance. Table 14 provides the results of the cold-side model performance calculations, while Figure 28 illustrates the relative changes in particle penetration for the various LNCFS conditions. The modeled ESP penetration increase for LNCFS 2 (the worst case) ranges from 9% for a small ESP to 35% for the largest ESP. The increased relative effect of changes in gas volume for cold-side ESPs than for the hot-side case is a result of the better overall performance of the cold-side units. That is, the better the performance of the ESP, the larger the degradation on a relative basis.

Although the specific values are somewhat different, in general the LNCFS conditions produced the same effects on both hot-side and cold-side ESP performance. It should be noted that although the highest relative increases in particle penetration resulted from the largest ESPs

modeled, the actual emission rates of these ESPs were so low that the effect might never be noticed. Figures 29 - 32 compare the particle emission rates and opacities calculated for all conditions and illustrate the actual magnitude of the changes.

4. SUMMARY OF RESULTS

A demonstration of the Low-NO_x combustion technology was conducted on the tangentially-fired boiler on Lansing Smith Unit 2. Three low-NO_x furnace configurations were compared to unmodified baseline operation to assess the effects on particulate control device performance. The following summary statements can be made about the results of the program.

The particle mass loadings exiting the furnace and entering the ESP were within the expected range predicted by the EPRI data base for the ash content of the coal burned. In general, only minor variations in mass loadings were observed between the test phases. At full load, the dry standard mass loadings were within 1 standard deviation of the mean of all tests. For all test phases, the average difference from the baseline mass loading was 6%. This is very little change, and is as likely to be related to coal characteristics or noise in the measurement as to low-NO_x modifications.

Fly ash particle size distributions were essentially identical for all boiler loads. Moreover, the measured distributions were typical of that predicted by the EPRI data base for pulverized-coal boilers burning bituminous coal. At full-load conditions, the size distributions for all phases of testing compared favorably, indicating that the low-NO_x modifications did not affect the size distribution of the fly ash. For the two lower loads, some differences were observed in the concentration of sub-micron particles between the various phases. However, the changes in size distribution were not consistent between the different tests and load conditions and are not believed to be meaningful.

The percentages of carbon and LOI in the LNCFS 3 samples were higher than for the other phases, particularly at the lower loads. After the coal mill overhaul, the LNCFS 3 ash carbon values were even higher. In most cases, carbon and LOI were somewhat higher on the South side of the ESP. Some of the LOI values for both sides of the ESP were high enough to possibly affect ESP emissions. Size segregated analysis of the mass train samples indicated that the carbon and LOI were mainly associated with particles larger than 200 mesh. Unfortunately, the relationship between the form, size, and concentration of carbon particles and the effect on ESP

performance is poorly understood, preventing an accurate assessment of the effects on ESP performance of the increase in LOI.

Some variations were observed in the vapor phase SO_3 concentration in the flue gas for various test phases. The variations appear to be directly related to the carbon content of the fly ash. The ash carbon content could be an indicator for changes in combustion conditions which cause increased SO_3 production in the furnace. Another explanation is that the carbon particles contribute to catalytic conversion of SO_2 to SO_3 in the convective heat transfer region of the boiler. This result is confused somewhat since the effect was not observed for the 180 MW baseline case, despite large changes in ash carbon content.

Laboratory measurements and predictive techniques indicated that no significant effect on the electrical resistivity of the fly ash occurred as a result of LNCFS. Differences between the baseline and LNCFS resistivity values were generally within a factor of 2 with various techniques disagreeing on greater differences. This is true for both hot-side and cold-side temperatures and for all boiler loads. A factor of 2 is the maximum practical resolution of the measurement. Significant performance effects are typically not observed with less than a factor of 5 change in resistivity.

Gas volume flow changes can have a significant effect on the performance of an ESP. Variations in measured gas flow between the test phases for a given boiler load were small, if differences in flue gas moisture and oxygen are ignored. Moisture content is primarily a function of the coal moisture and not a combustion effect. Some changes in gas temperature were observed, but these changes were also small and appeared to be seasonably related to the ambient temperatures. The main effect on gas flow was related to the oxygen content of the flue gas, which does appear to be related to the low-NO_x operation. The long-term flue gas oxygen data indicated differences which would affect ESP performance by changing the gas volume flow. Based on the oxygen content alone, the gas volume for LNCFS 2 and 3 should be greater than the baseline case by 5% and 3%, respectively. The LNCFS 1 volume should be 3% less than the baseline.

ESP performance modeling was performed on the assumption that the only differences between the test phases were the gas volume changes caused by the measured differences in long-term oxygen levels. Otherwise, all test phases were assumed to have the same operating conditions as the baseline condition. Projections were made for a series of hypothetical ESPs with SCA values ranging from 150 to 500 ft^2/1000 acfm. Hot-side modeling results showed that LNCFS 2 operation is expected to increase the ESP particle penetration over the baseline values by from 8% for a small ESP to 27% for a large ESP. For LNCFS 3 operation, the increase is from 5 to 19% for small and large ESPs. For LNCFS 1 operation, the ESP particle penetration is reduced from the baseline levels by from 4% for a small ESP to 13% for a large ESP. Because of basic differences in their natures, the projected performance of the cold-side ESPs was significantly better than the hot-side units for all cases. Because of the lower overall emissions, the changes produced by the volume flow increases resulted in higher relative changes. The model predicted penetration increases of 9% to 35% for LNCFS 2 and 7% to 25% for LNCFS 3. The reduced oxygen during LNCFS 1 reduced penetration by 6% to 17%.

5. REFERENCES

1. R. R. Hardman, L. L. Smith, and S. Tavoularcas. Results from the IDDT T-Fired Demonstration Project Including the Effect of Coal Fineness of NO_x Emissions and Unburned Carbon Levels. Presented at the EPRI/EPA 1993 Joint Symposium on Stationary Combustion NO_x Control, Miami Beach, FL, May 24-27, 1993.

2. J. L. DuBard and R. S. Dahlin. Precipitator Performance Estimating Procedure. EPRI Report CS-5040, RP629-5. Electric Power Research Institute, Palo Alto, CA, 1987.

3. R. E. Bickelhaupt. A Study to Improve A Technique for Predicting Fly Ash Resistivity with Emphasis on the Effect of Sulfur Trioxide. EPA 600/7-86-010, NTIS PB86-178126. U.S. Environmental Protection Agency, IERL, Research Triangle Park, NC, 1985.

4. E. L. Merryman and A Levy. Enhanced SO_3 Emissions from Staged Combustion. U.S. Environmental Protection Agency, Research Triangle Park, NC. EPA-600/7-79-002. January 1979.

5. J. G. Calvert. SO_2, NO, and NO_2 Oxidation Mechanisms. Acid Precipitation Series Volume 2. Butterworth Publishers, Stoneham, MA. 1984.

6. R. E. Bickelhaupt. An Interpretation of the Deteriorative Performance of Hot-Side Precipitators. JAPCA 30(8) 882-888, 1980.

7. R. E. Bickelhaupt, et al. Sodium Conditioning for Improved Hot-Side Precipitator Performance - Volume 1. EPRI Report CS-3711, RP724-2. Electric Power Research Institute, Palo Alto, CA, 1984.

8. R. E. Bickelhaupt. A Method for Predicting the Effective Volume Resistivity of Sodium-Depleted Fly Ash Layers in Hot-Side Electrostatic Precipitators. EPRI Report CS-3421, RP724-2. Electric Power Research Institute, Palo Alto, CA, 1984.

9. M. G. Faulkner and J. L. DuBard. A Mathematical Model of Electrostatic Precipitation (Revision 3). U.S. Environmental Protection Agency, Research Triangle Park, NC. EPA-600/7-84-069a,b,c. June 1984.
   Volume I, Modeling and Programming. NTIS PB84-212-679
   Volume II, User Manual. NTIS PB84-212-687
   FORTRAN Source Code Tape. NTIS PB84-232-990

10. S. Oglesby and G. B. Nichols. Electrostatic Precipitation. Marcel Dekker, New York, NY. 1978.

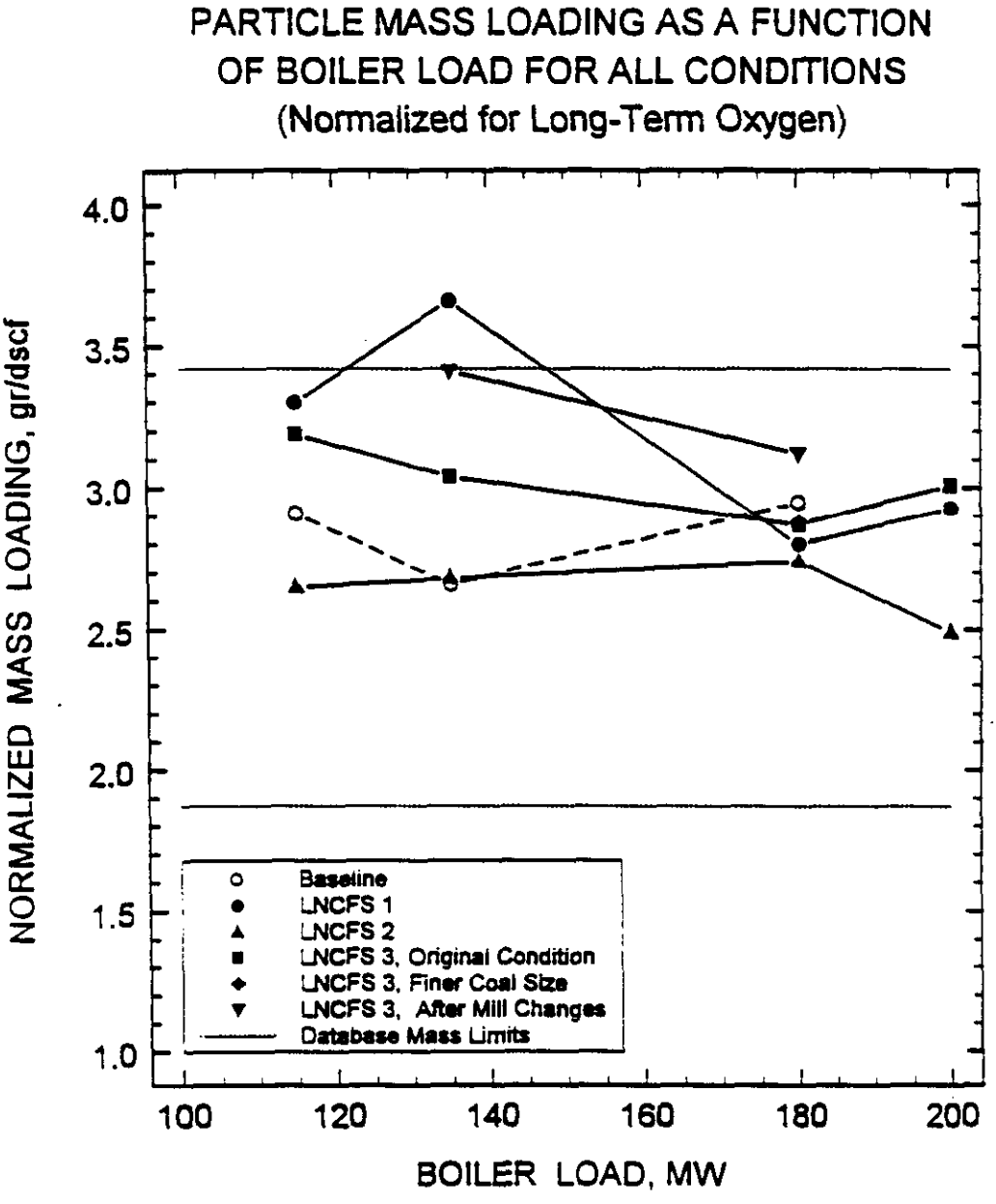

Figure 1. ESP Inlet Particle Mass Loading as a Function of Boiler Load.

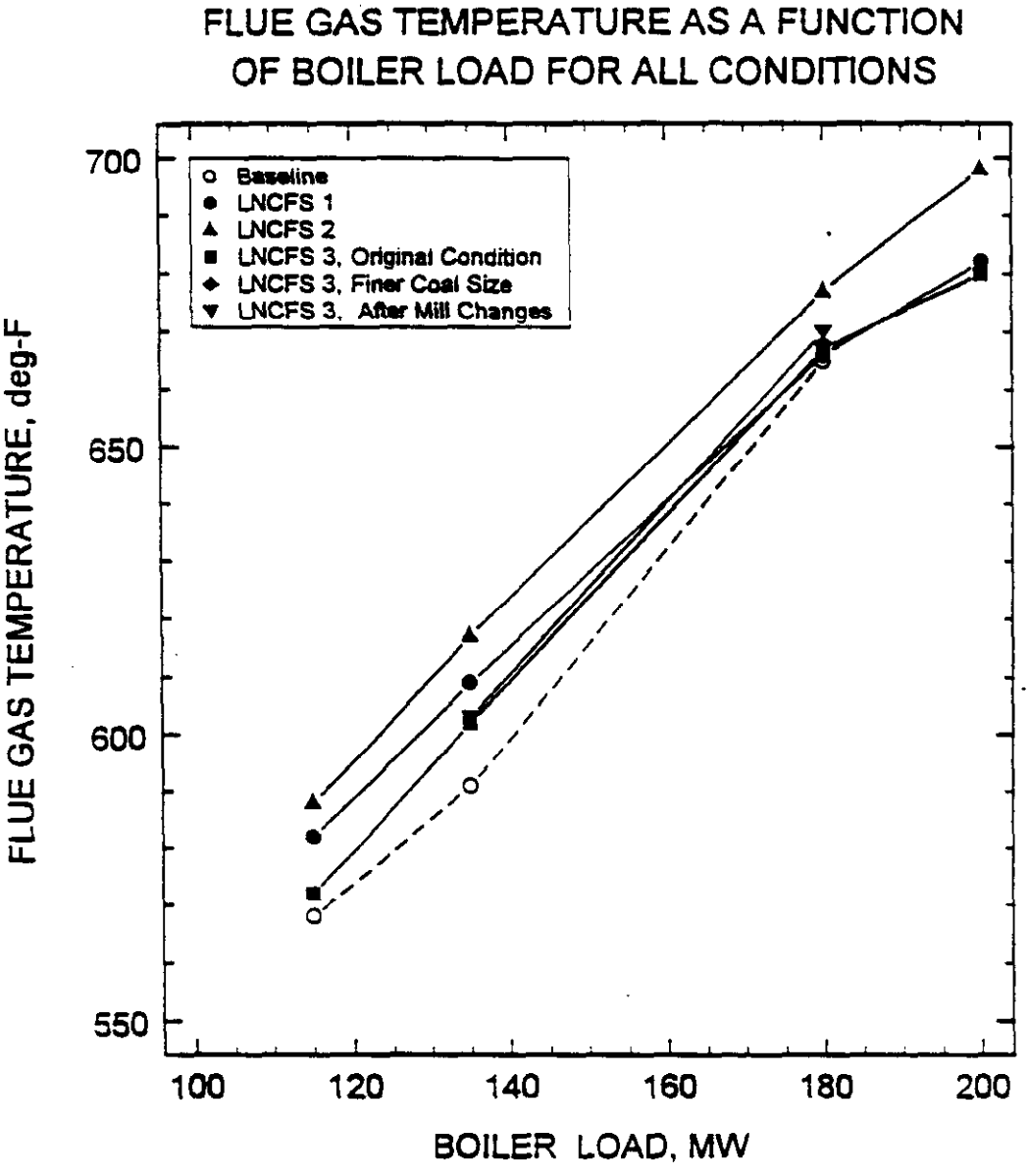

Figure 2. ESP Inlet Flue Gas Temperature as a Function of Boiler Load.

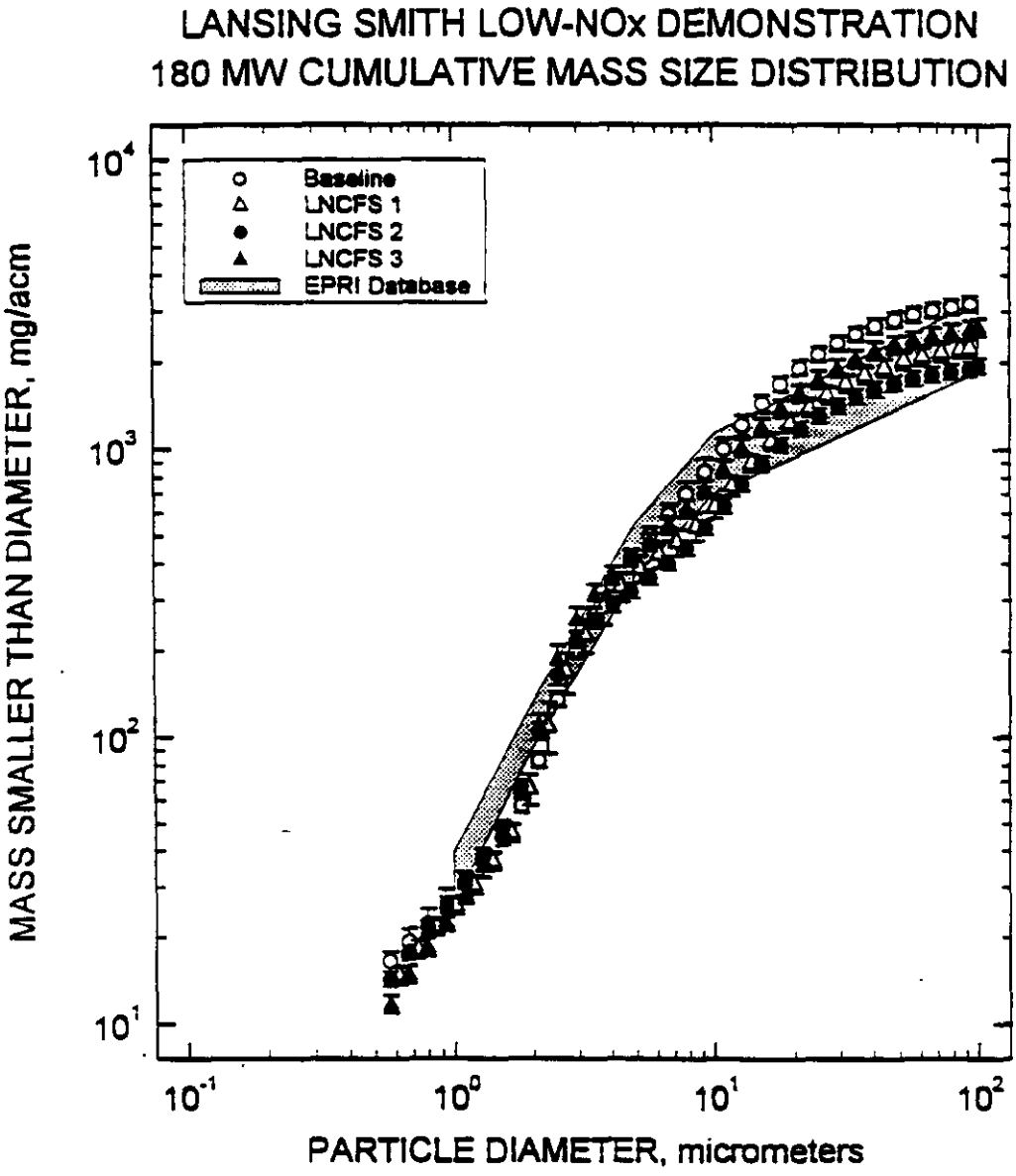

Figure 3. ESP Inlet Cumulative Mass Particle Size Distribution for 180 MW.

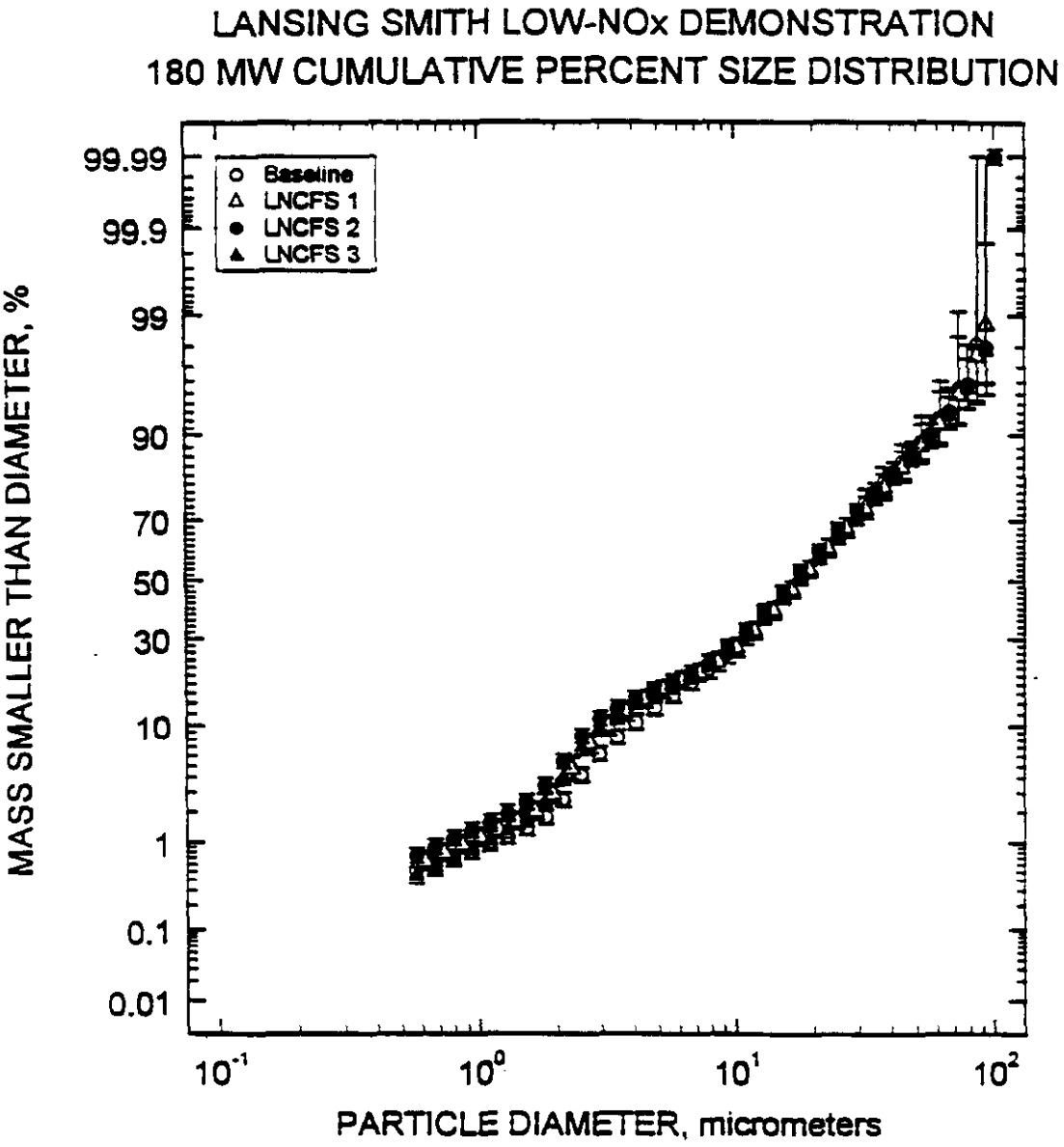

Figure 4. ESP Inlet Cumulative Percent Particle Size Distribution for 180 MW.

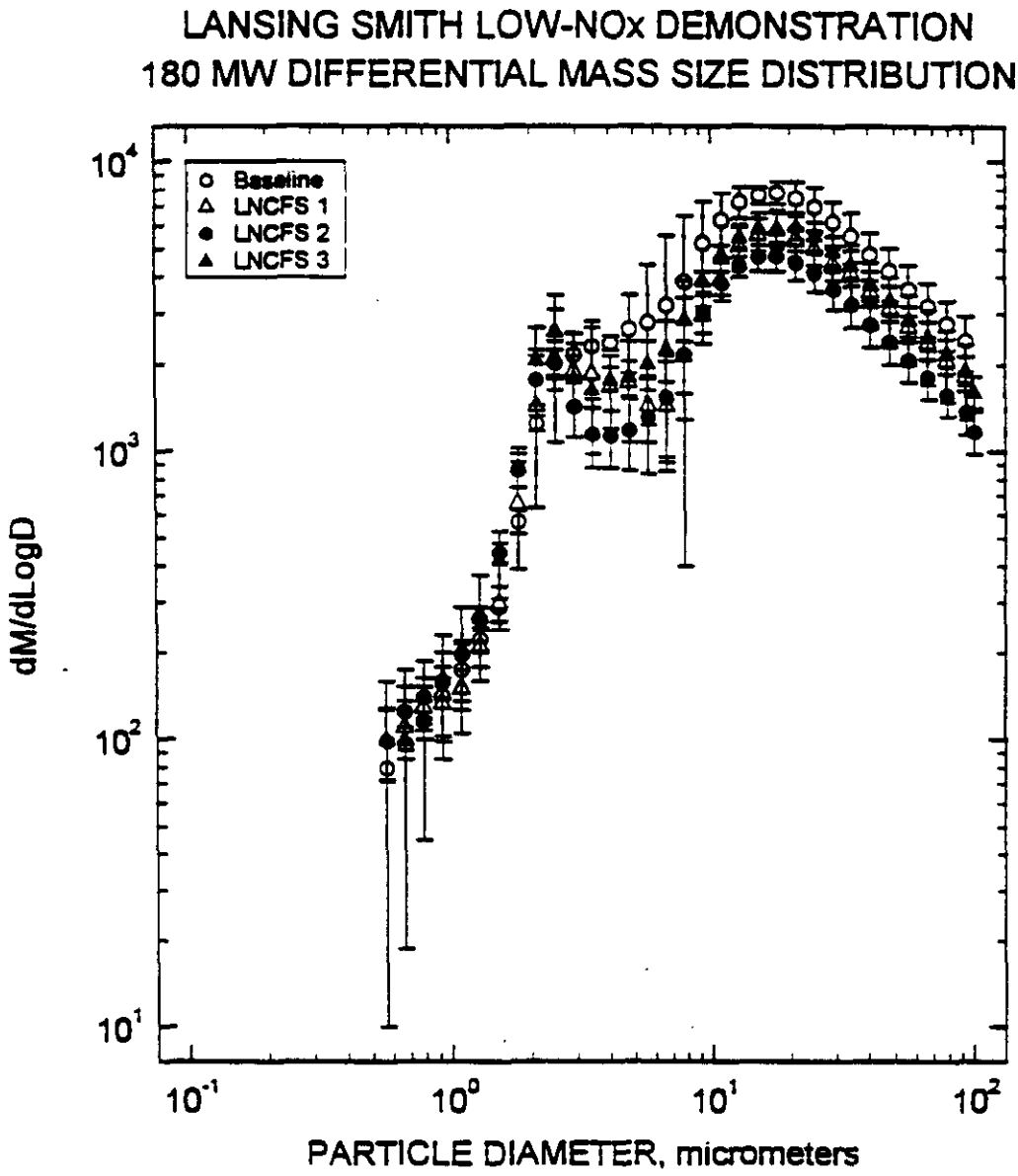

Figure 5. ESP Inlet Differential Mass Particle Size Distribution for 180 MW.

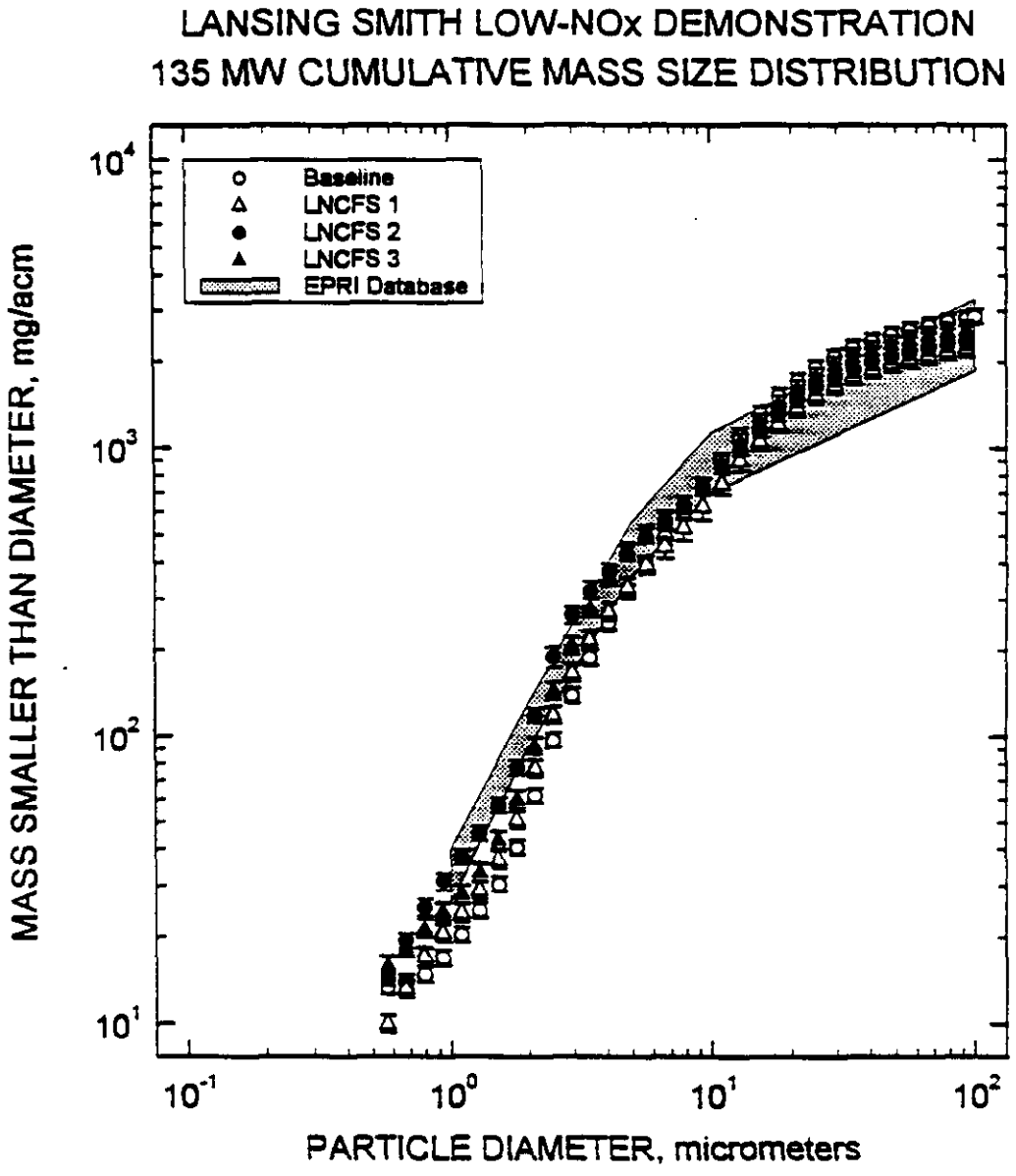

Figure 6. ESP Inlet Cumulative Mass Particle Size Distribution for 135 MW.

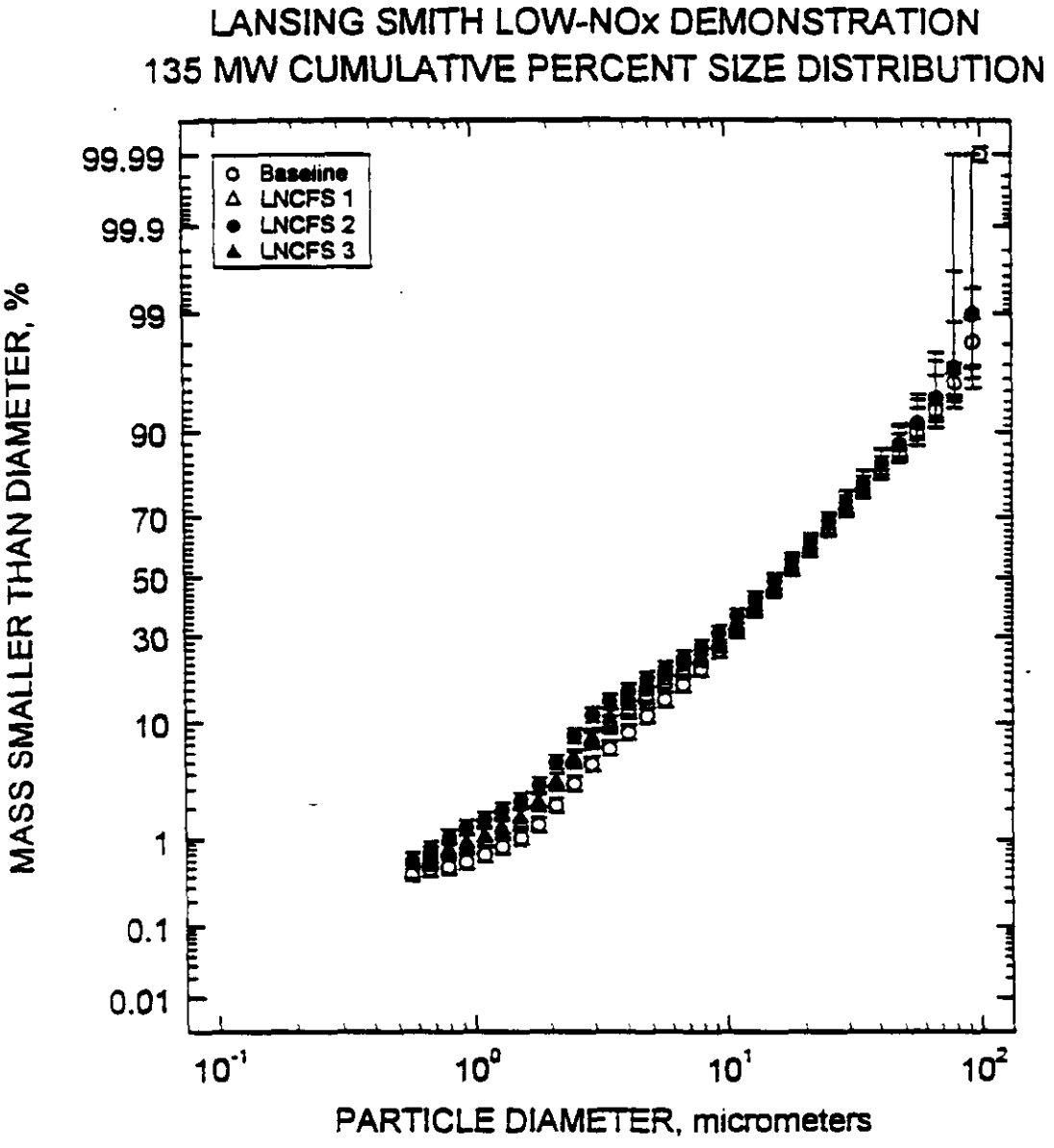

Figure 7. ESP Inlet Cumulative Percent Particle Size Distribution for 135 MW.

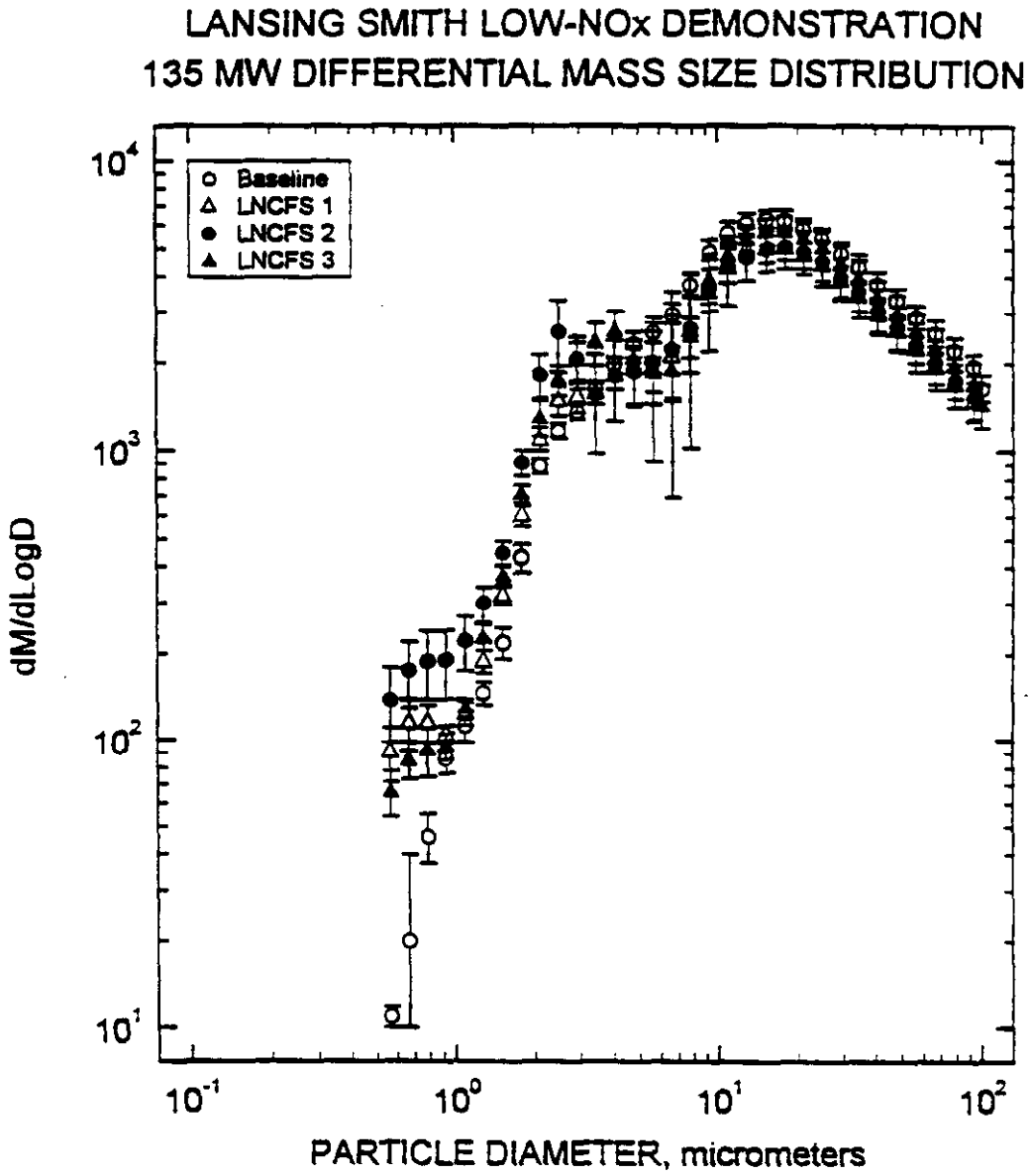

Figure 8. ESP Inlet Differential Mass Particle Size Distribution for 135 MW.

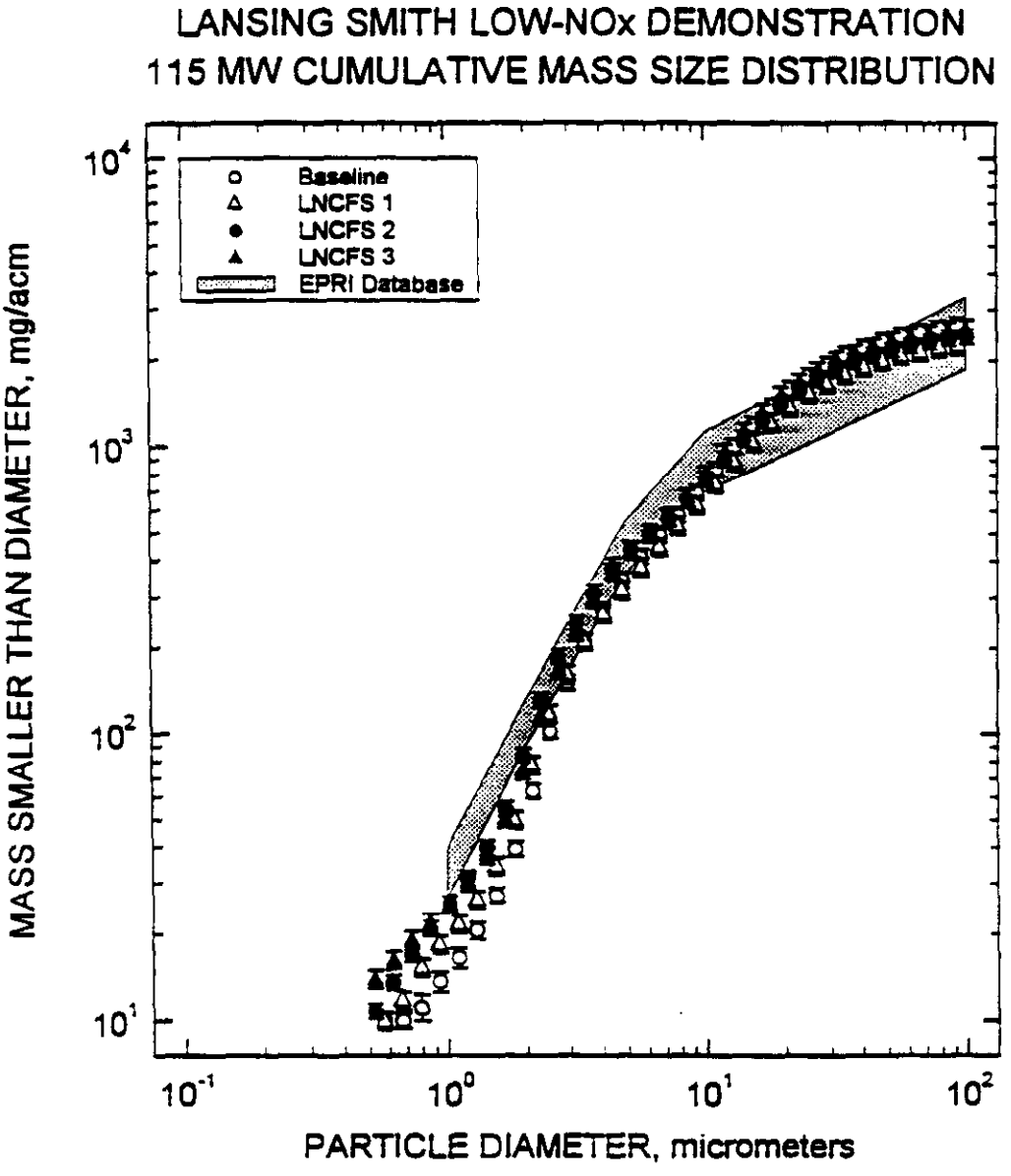

Figure 9. ESP Inlet Cumulative Mass Particle Size Distribution for 115 MW.

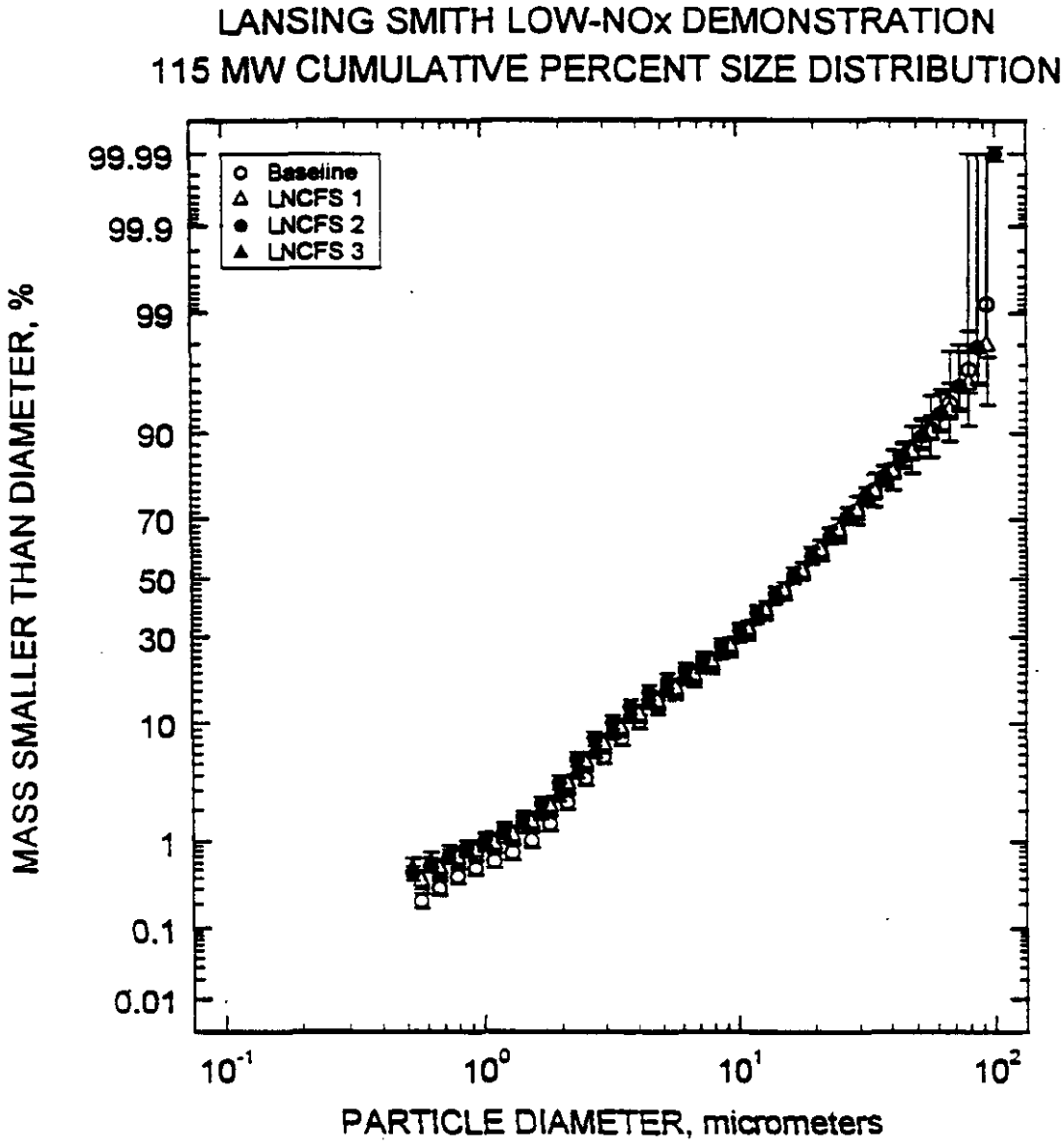

Figure 10. ESP Inlet Cumulative Percent Particle Size Distribution for 115 MW.

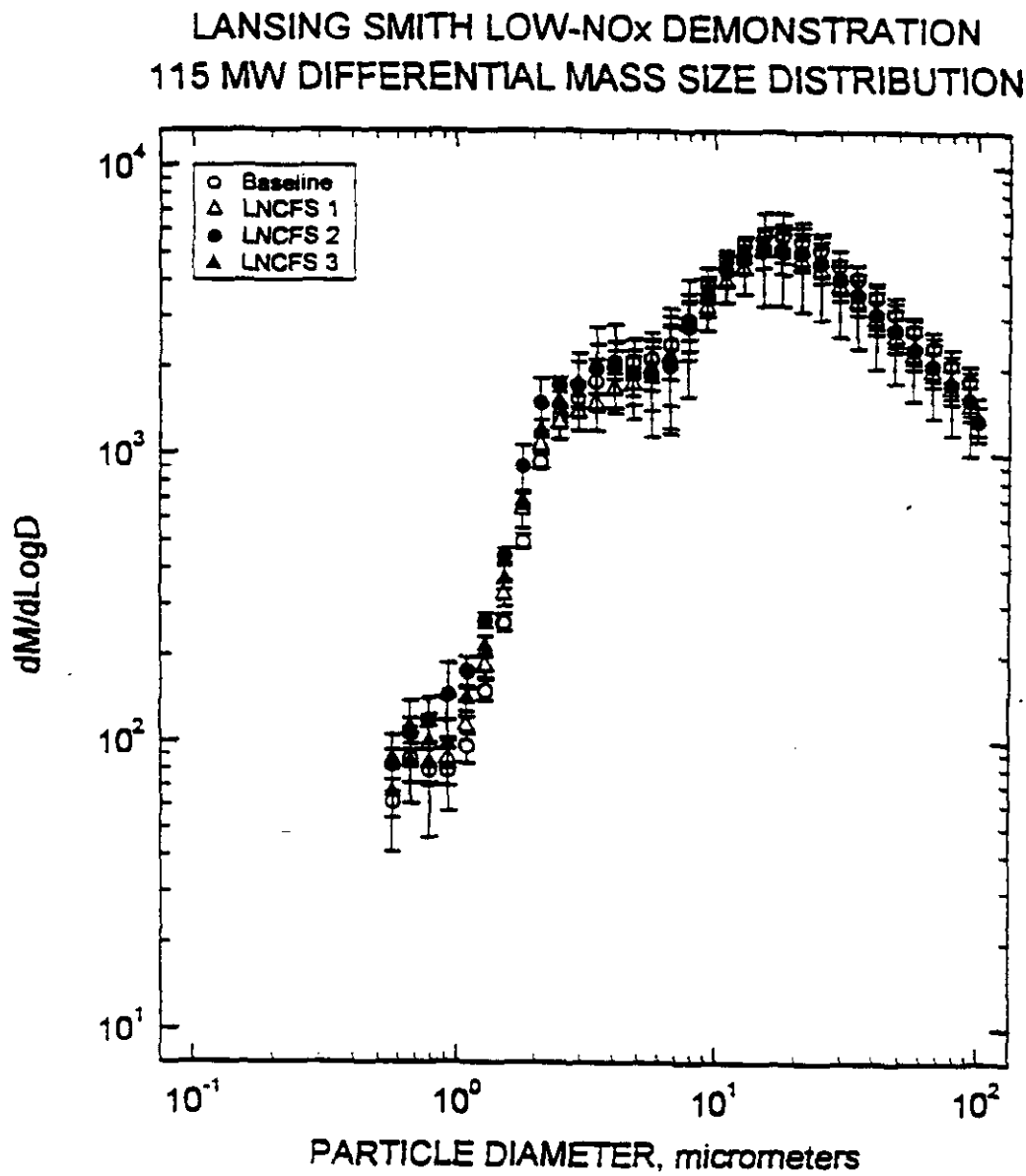

Figure 11. ESP Inlet Differential Mass Particle Size Distribution for 115 MW.

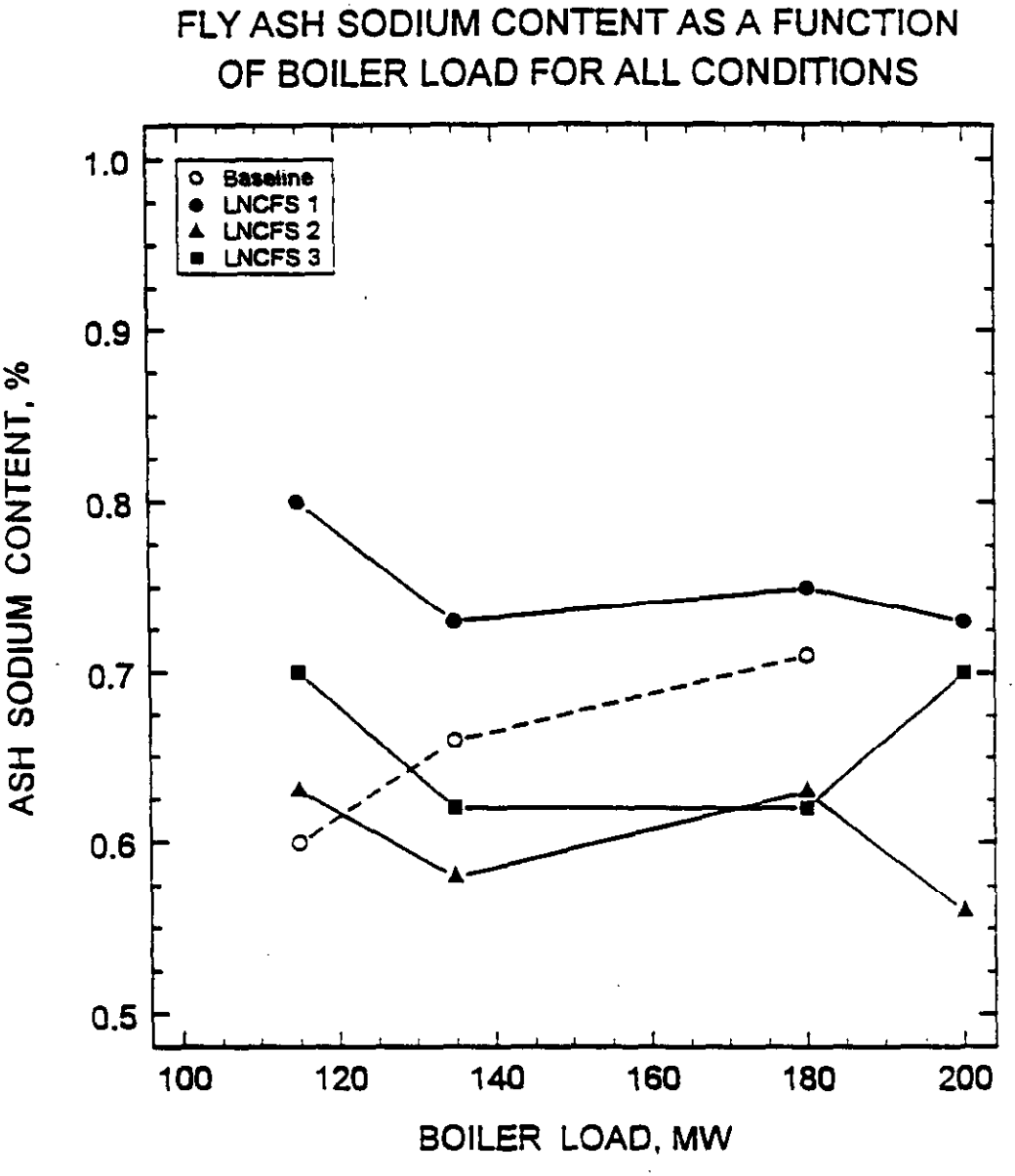

Figure 12. Fly Ash Sodium Content as a Function of Boiler Load.

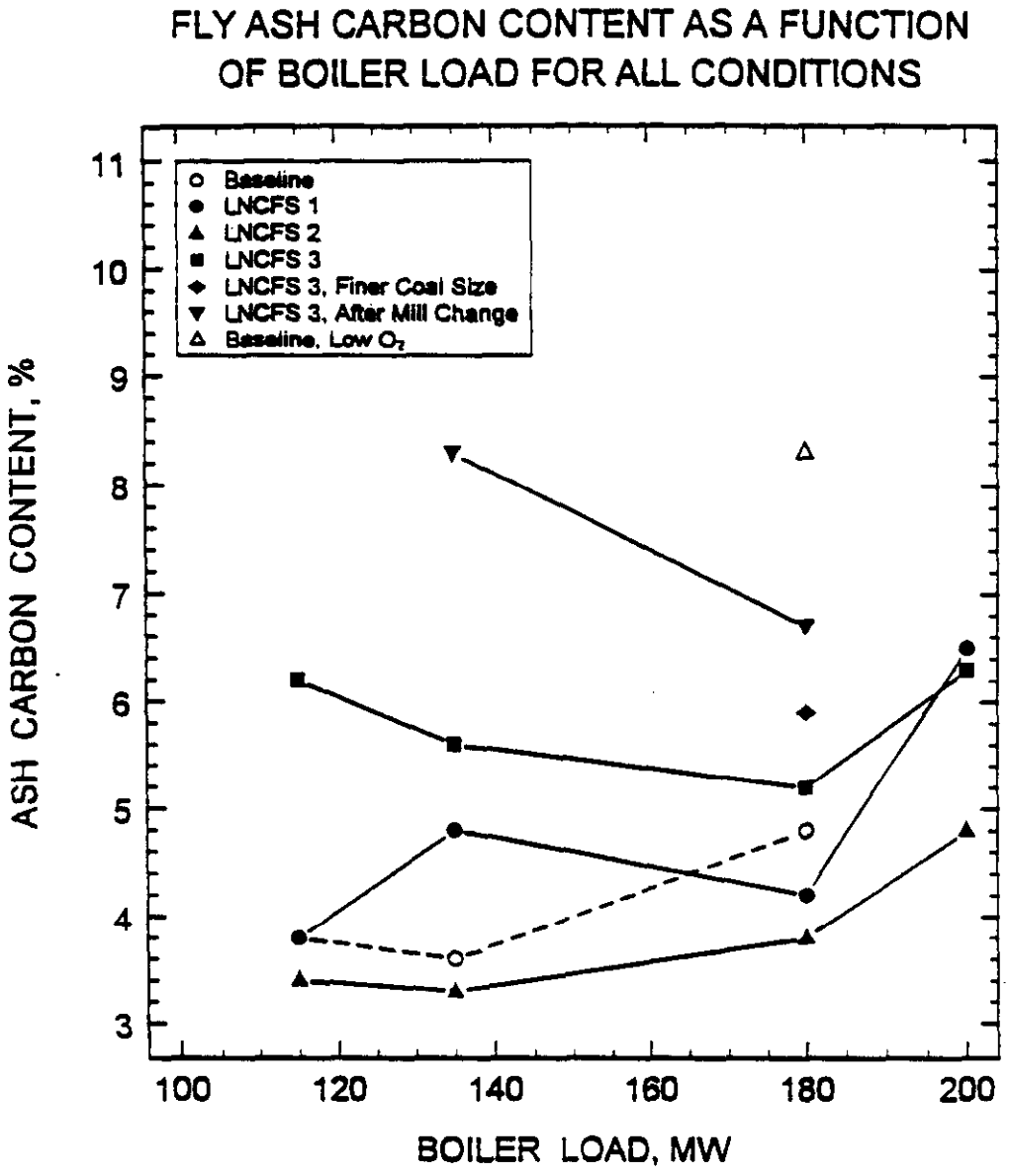

Figure 13. Fly Ash Carbon Content as a Function of Boiler Load.

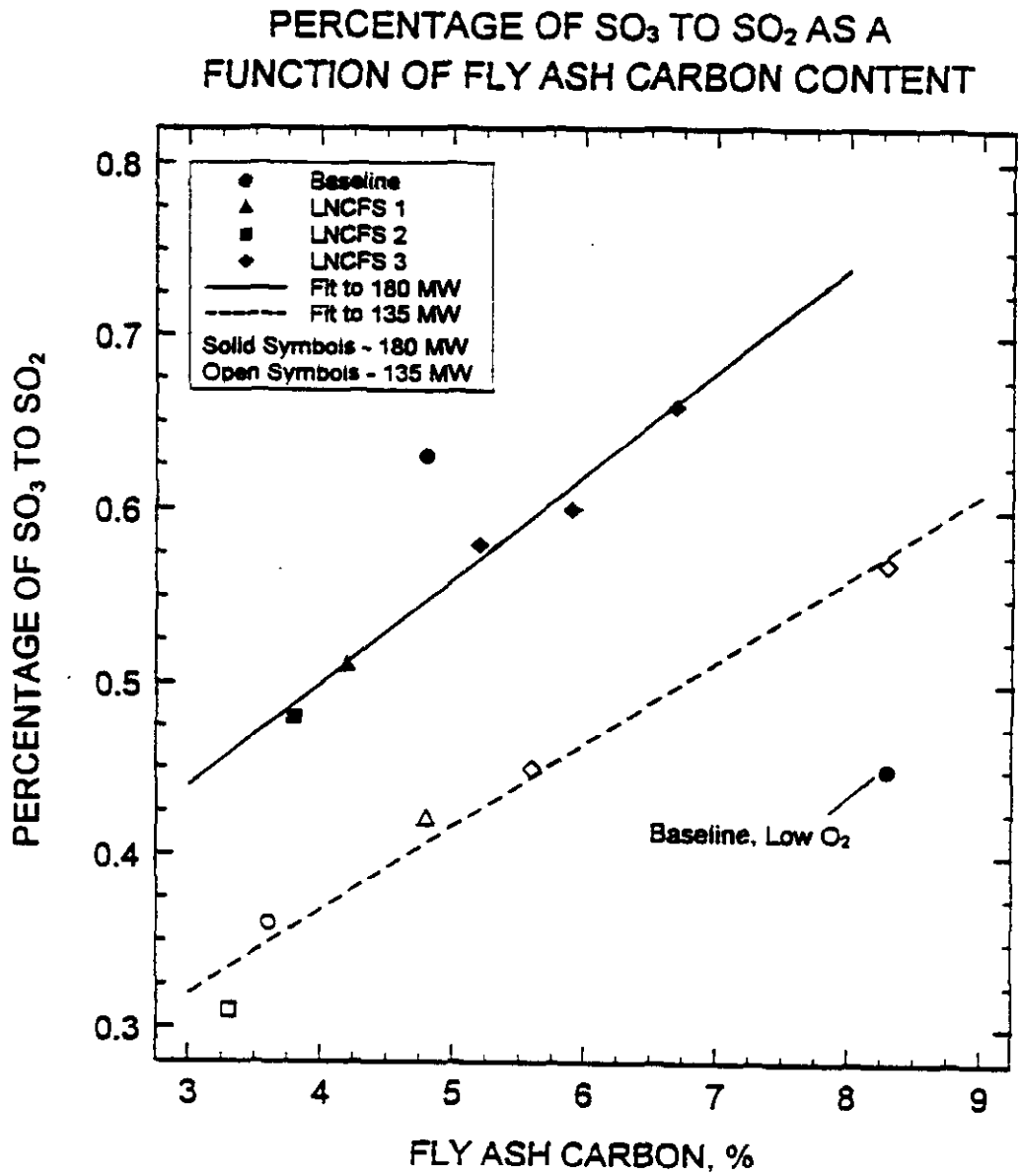

Figure 14. Percentage of SO_3 to SO_2 as a Function of Fly Ash Carbon Content.

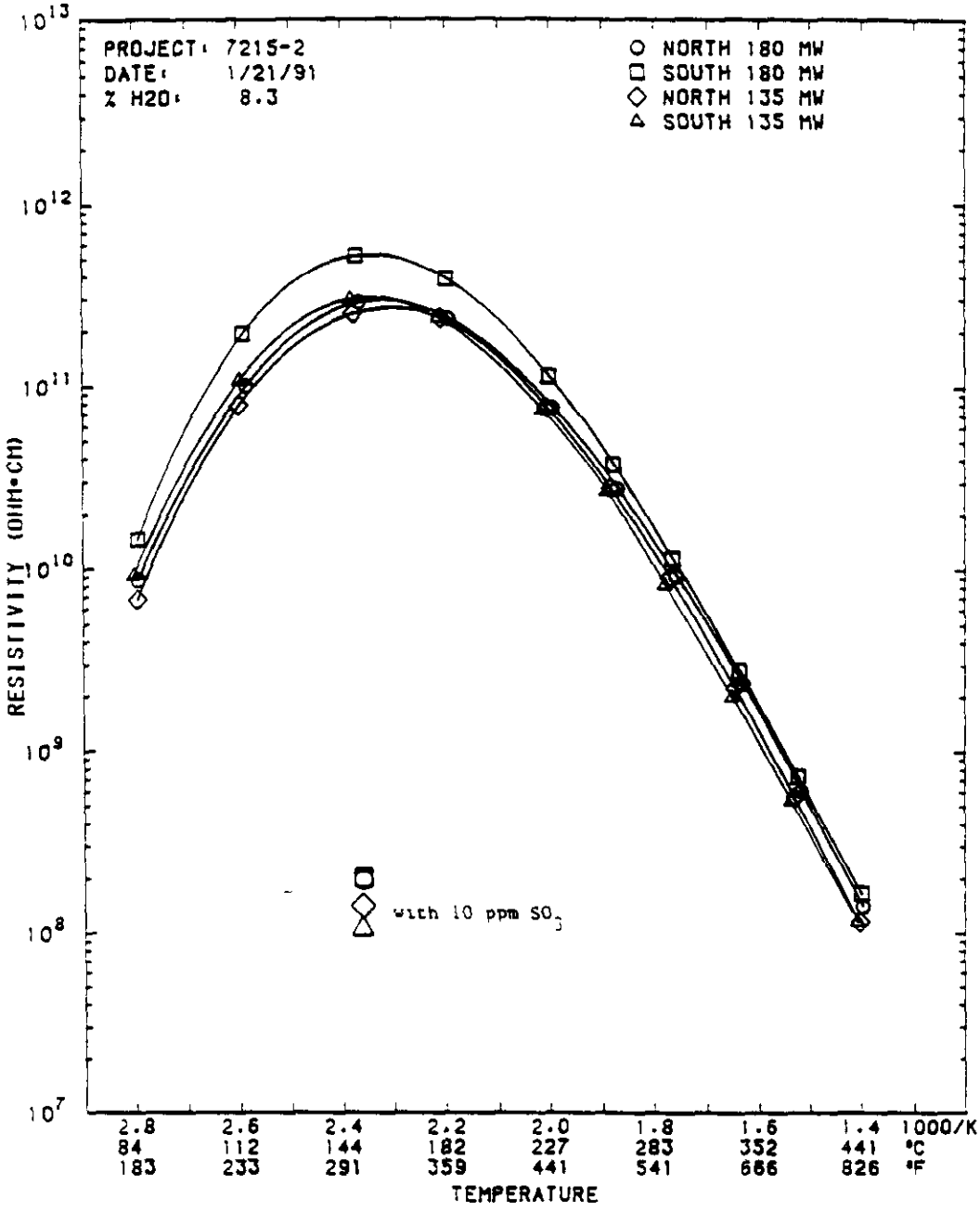

Figure 15. Fly Ash Resistivity For 180 MW (Low O_2) and 135 MW Baseline Tests.

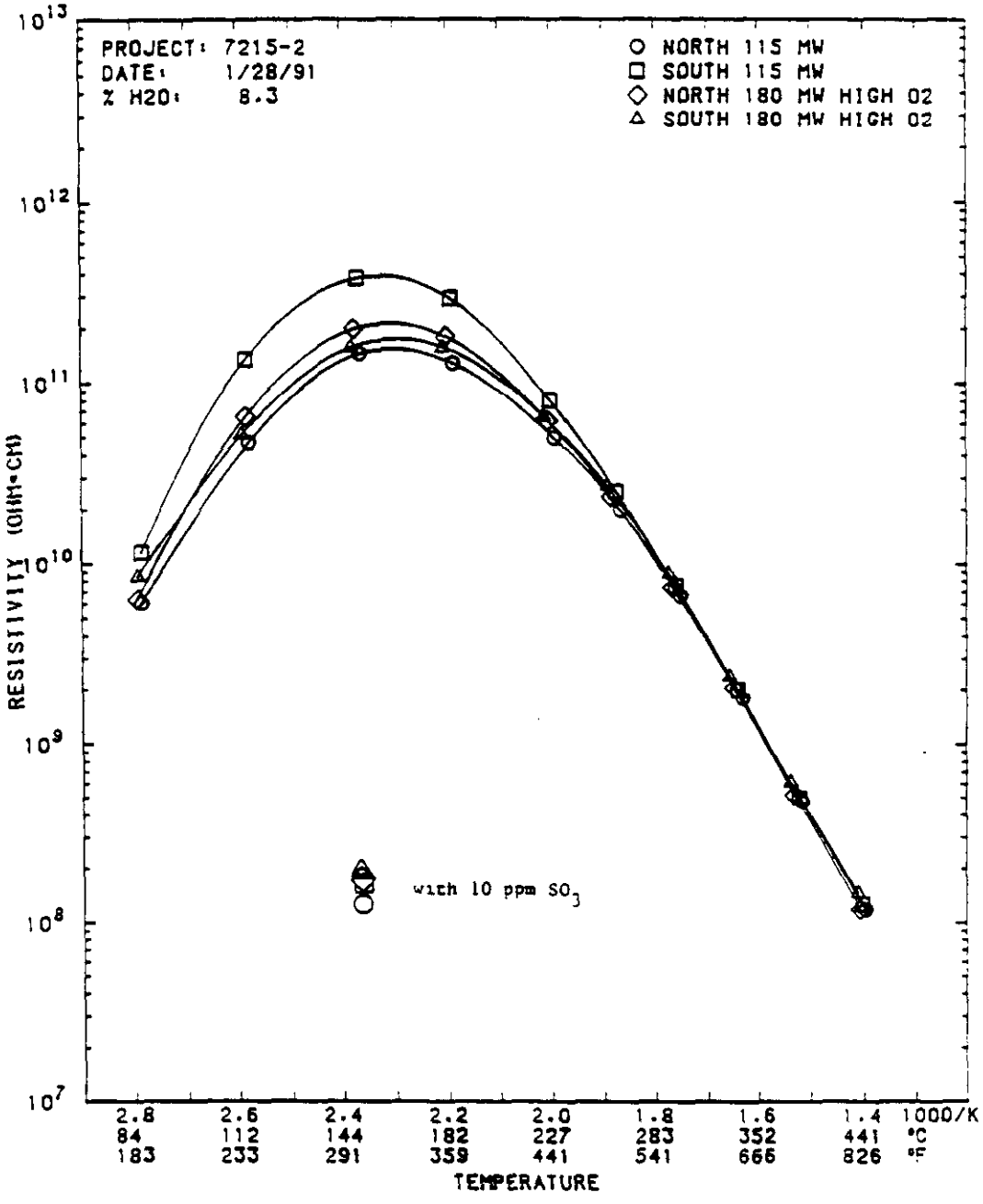

Figure 16. Fly Ash Resistivity For 115 MW and 180 MW (Normal O_2) Baseline Tests.

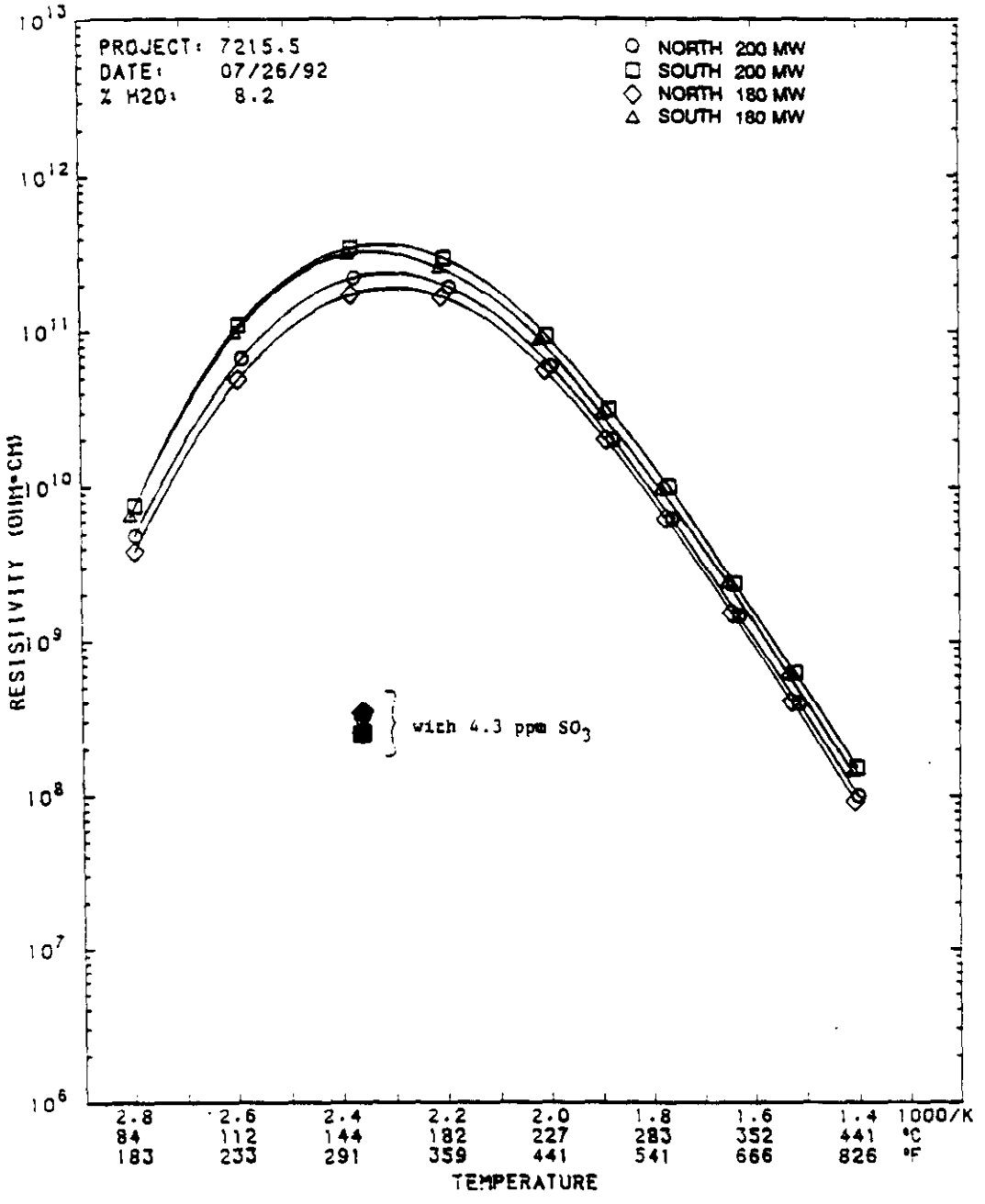

Figure 17. Fly Ash Resistivity For 200 MW and 180 MW LNCFS 1 Tests.

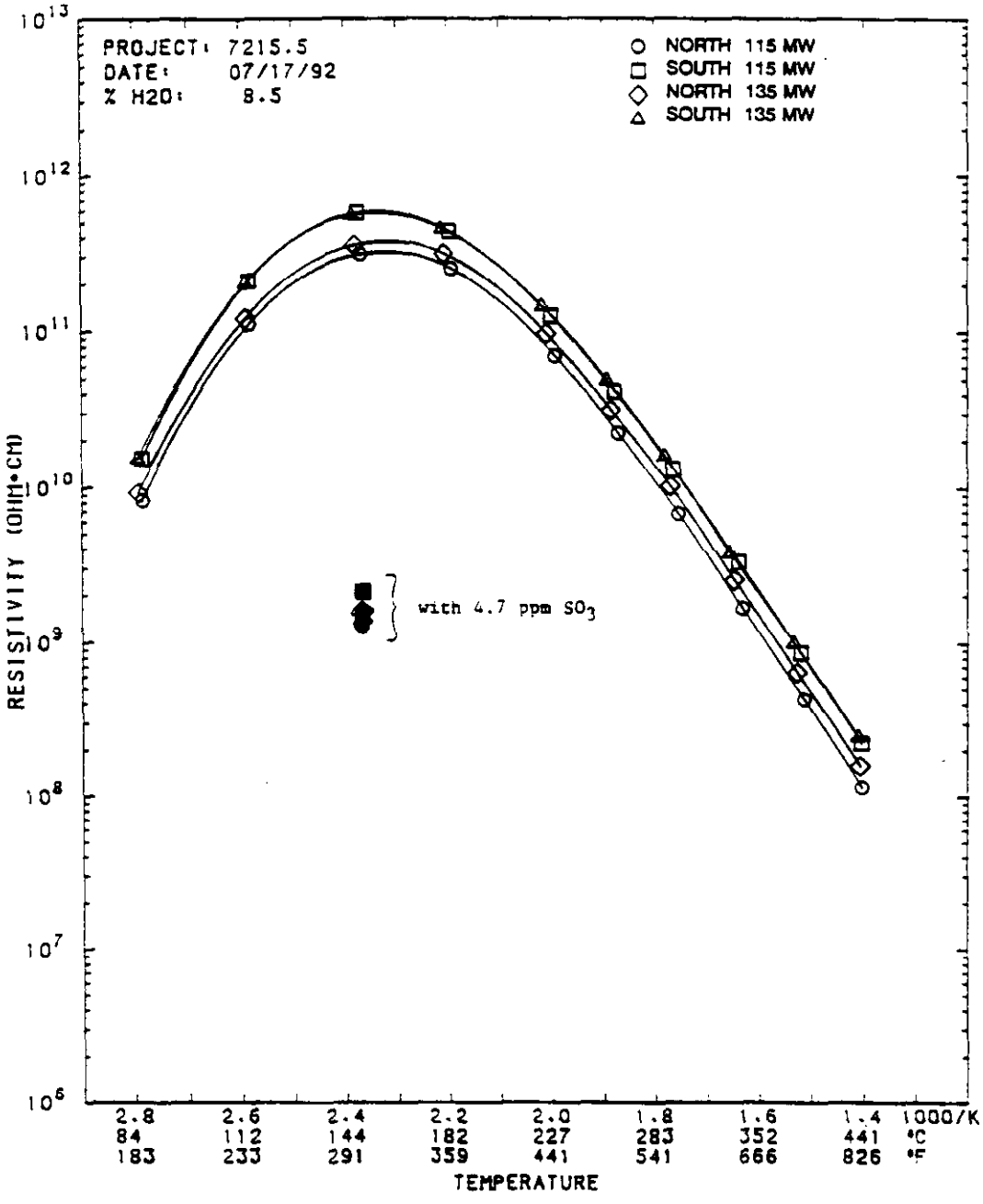

Figure 18. Fly Ash Resistivity For 135 MW and 115 MW LNCFS 1 Tests.

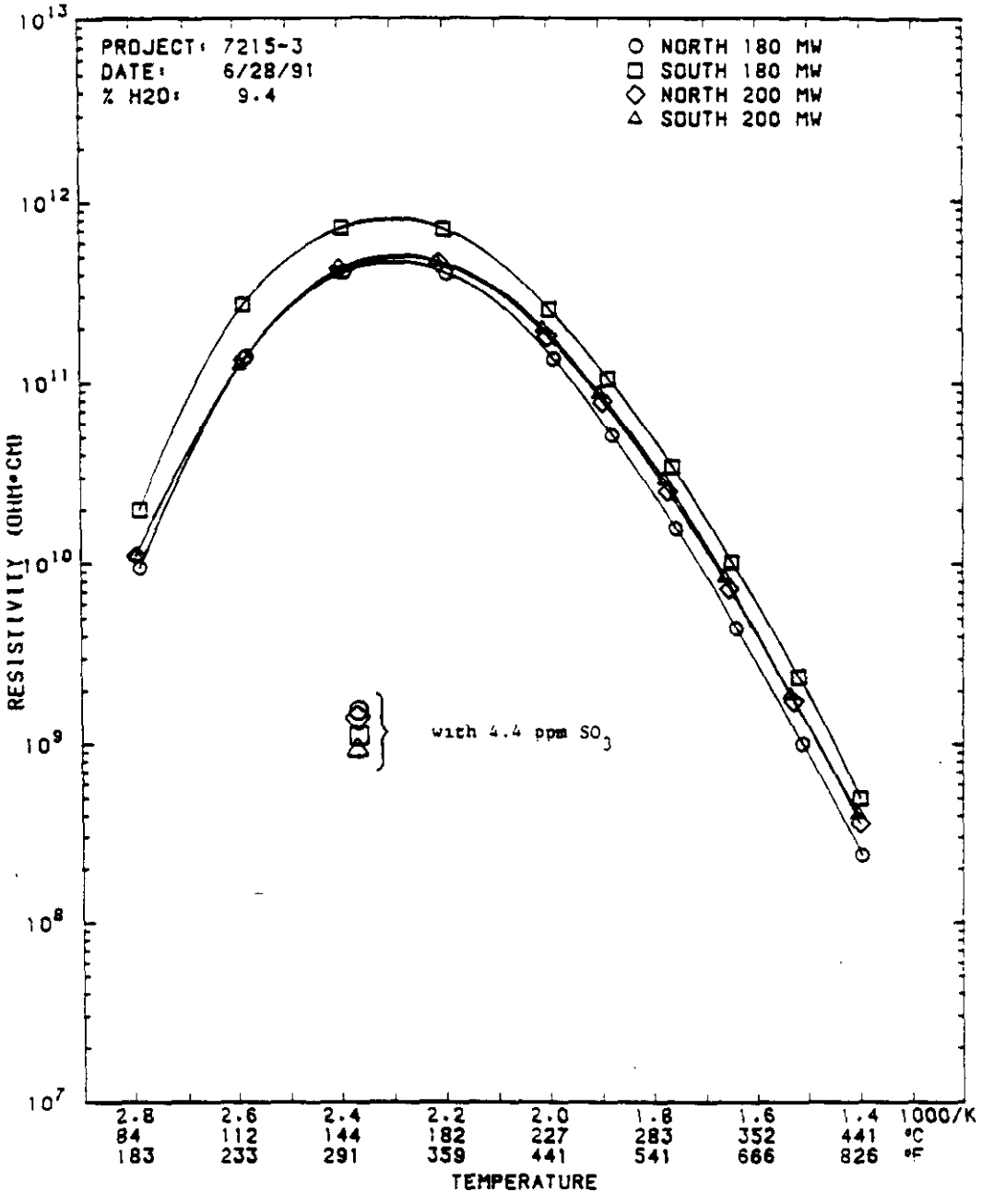

Figure 19. Fly Ash Resistivity For 200 MW and 180 MW LNCFS 2 Tests.

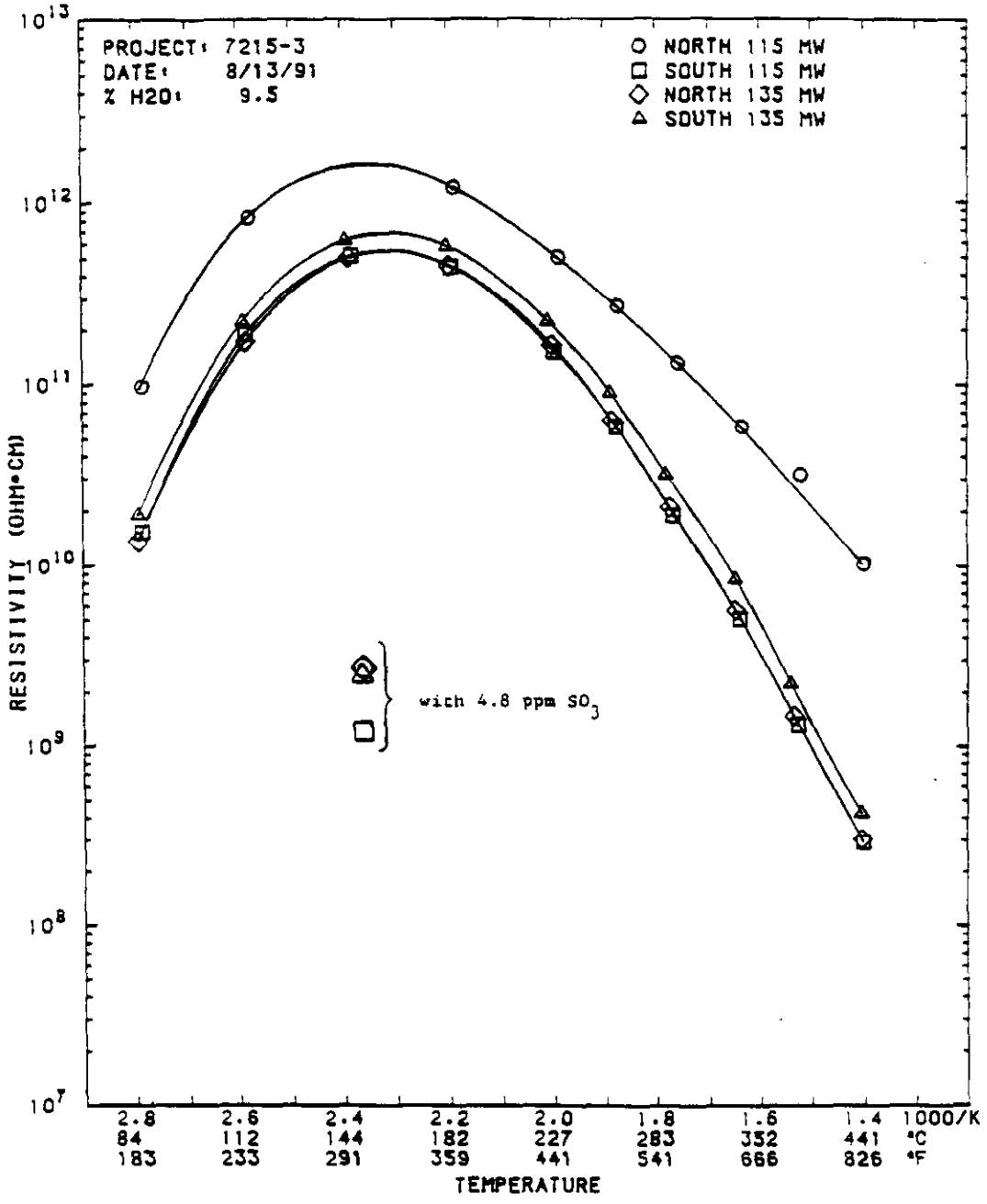

Figure 20. Fly Ash Resistivity For 135 MW and 115 MW LNCFS 2 Tests.

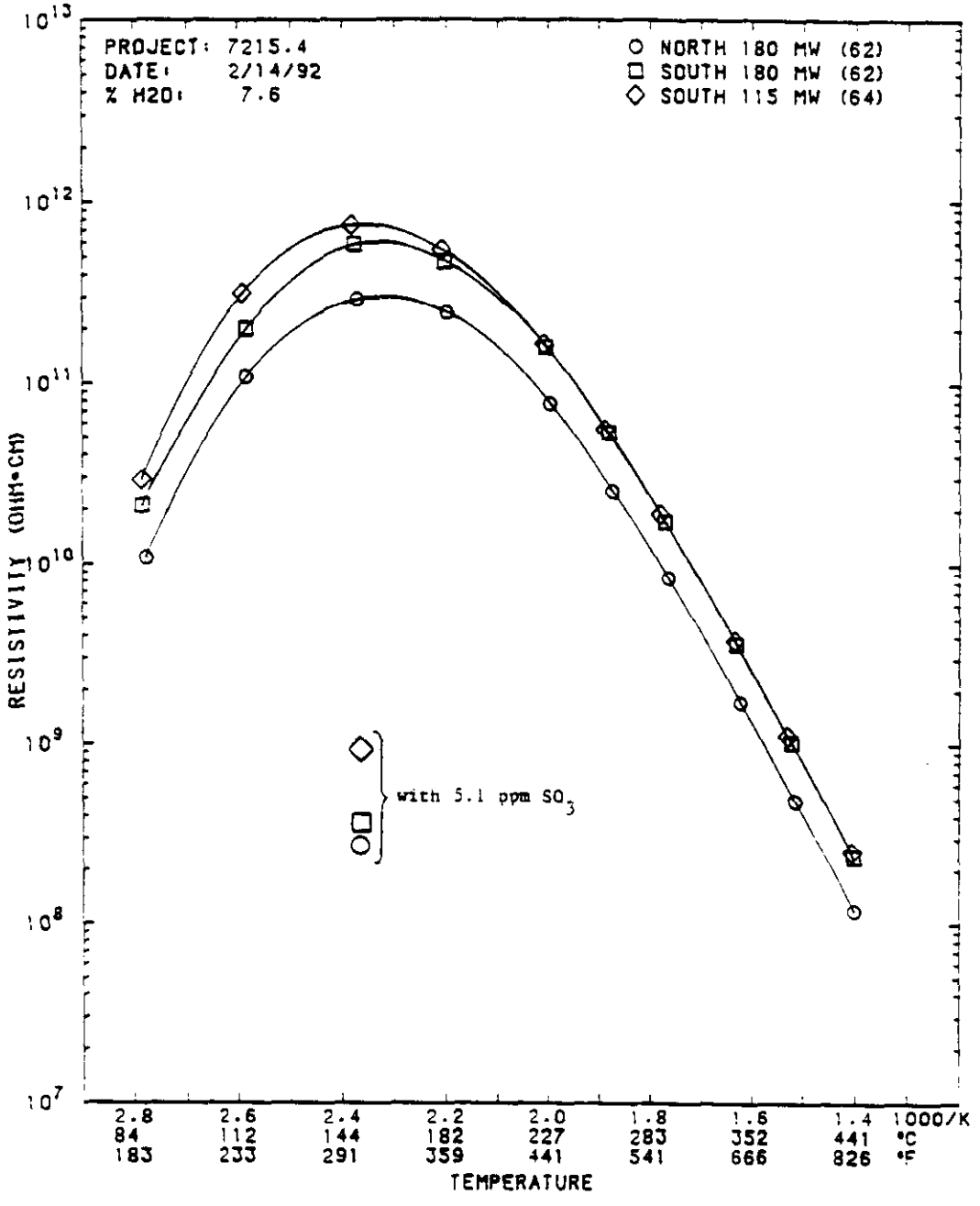

Figure 21. Fly Ash Resistivity For 180 MW and 115 MW LNCFS 3 Tests.

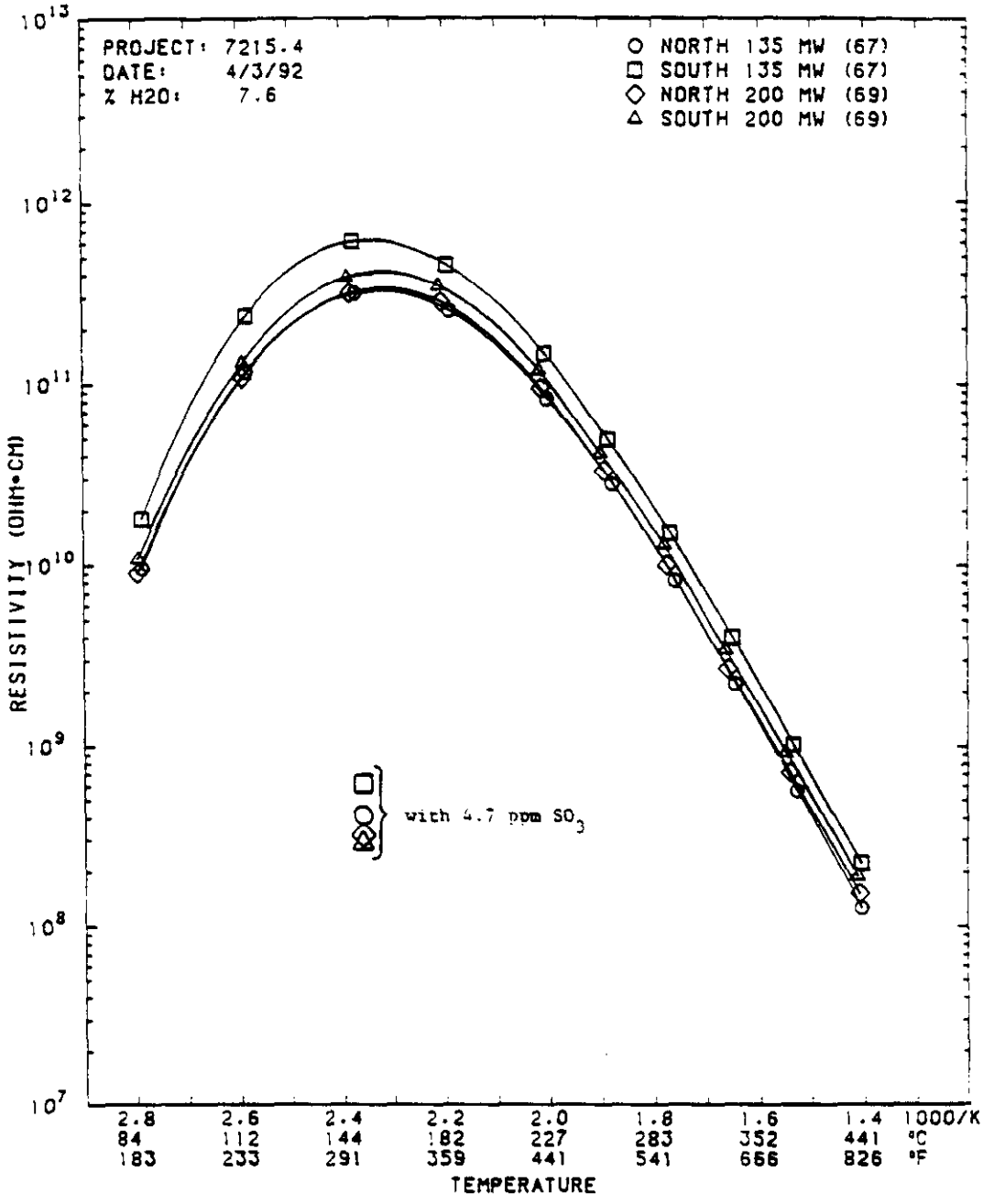

Figure 22. Fly Ash Resistivity For 135 MW and 200 MW LNCFS 3 Tests.

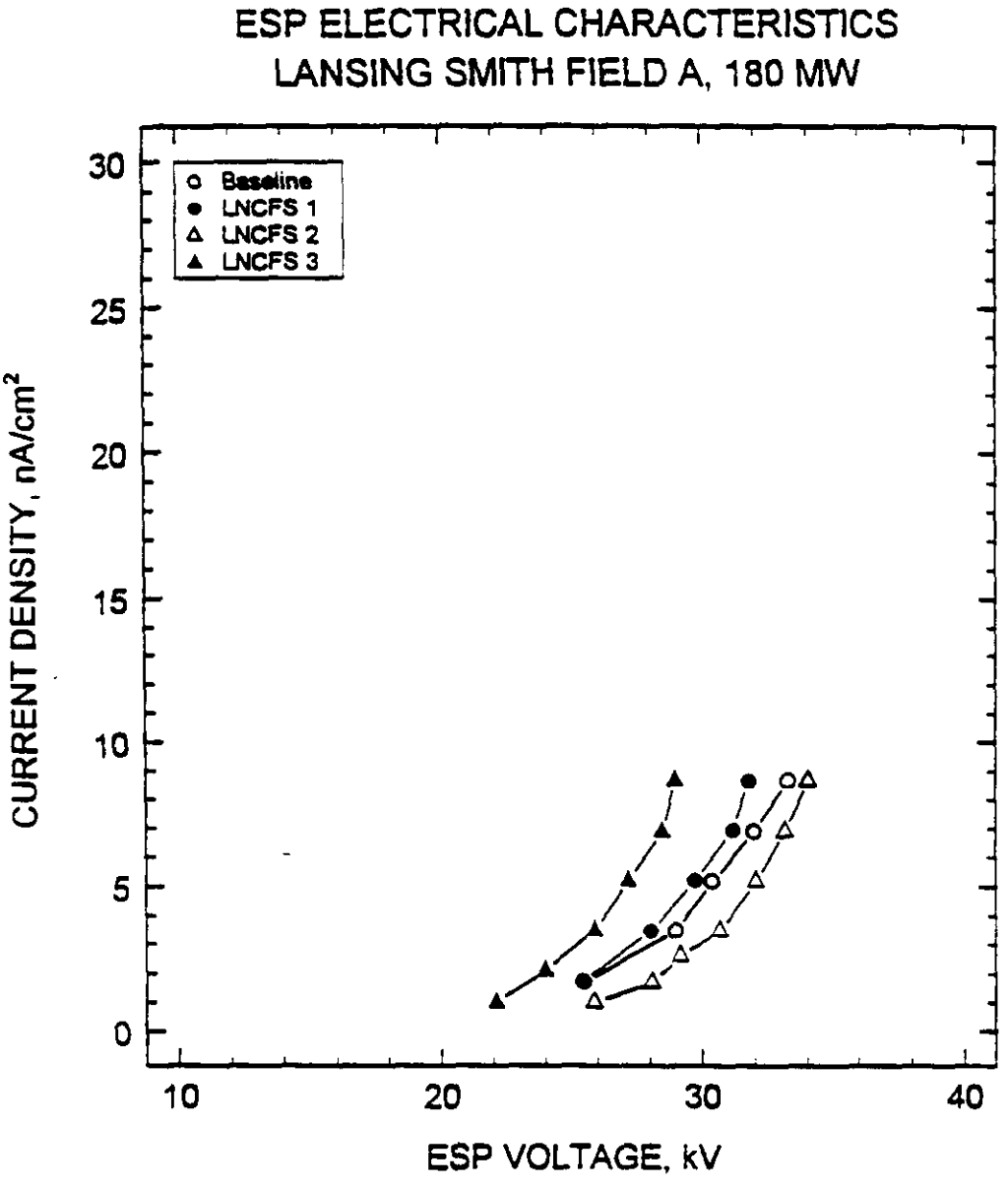

Figure 23. Inlet Field ESP Electrical Characteristics from All Test Phases.

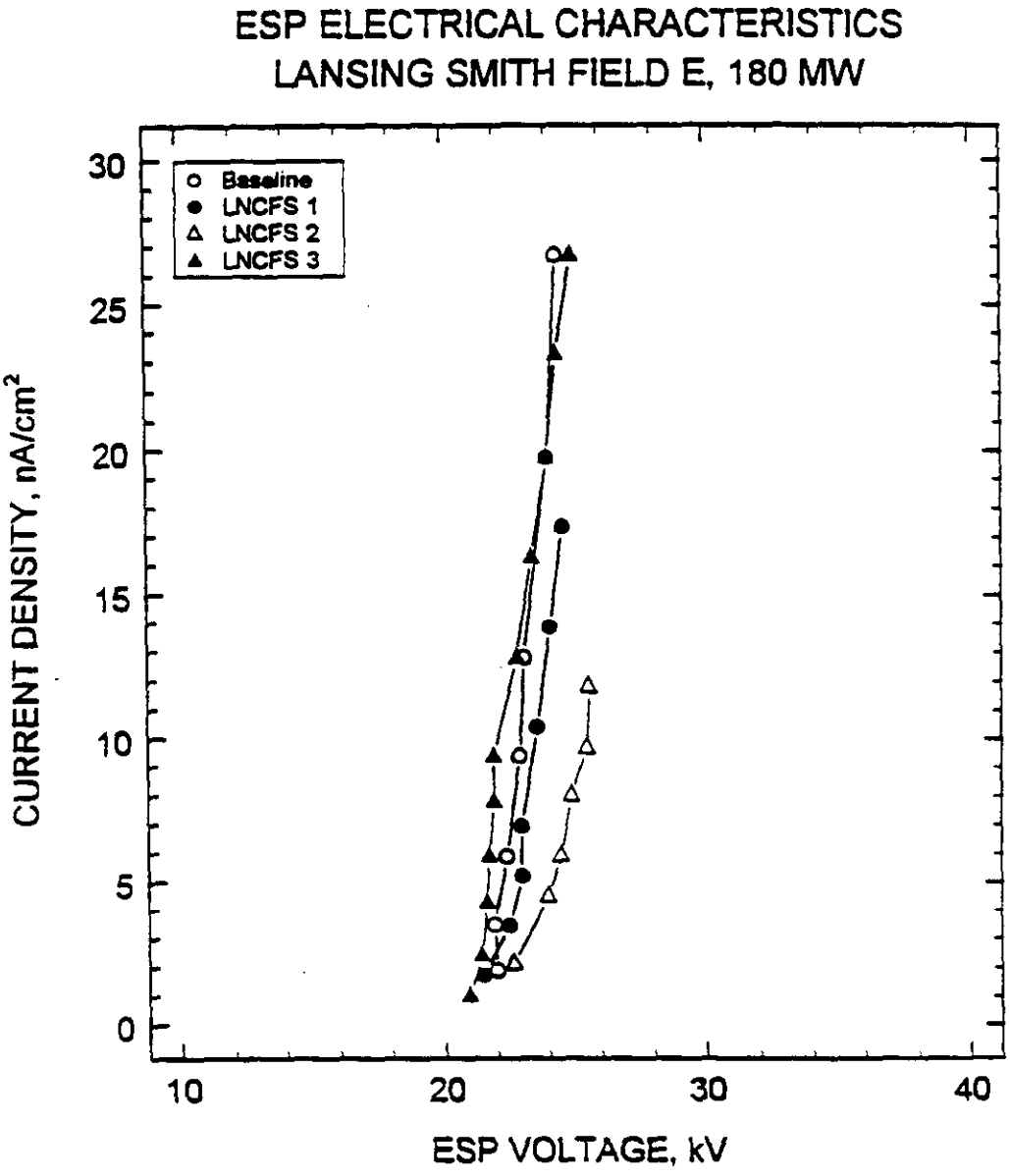

Figure 24. Third Field ESP Electrical Characteristics from All Test Phases.

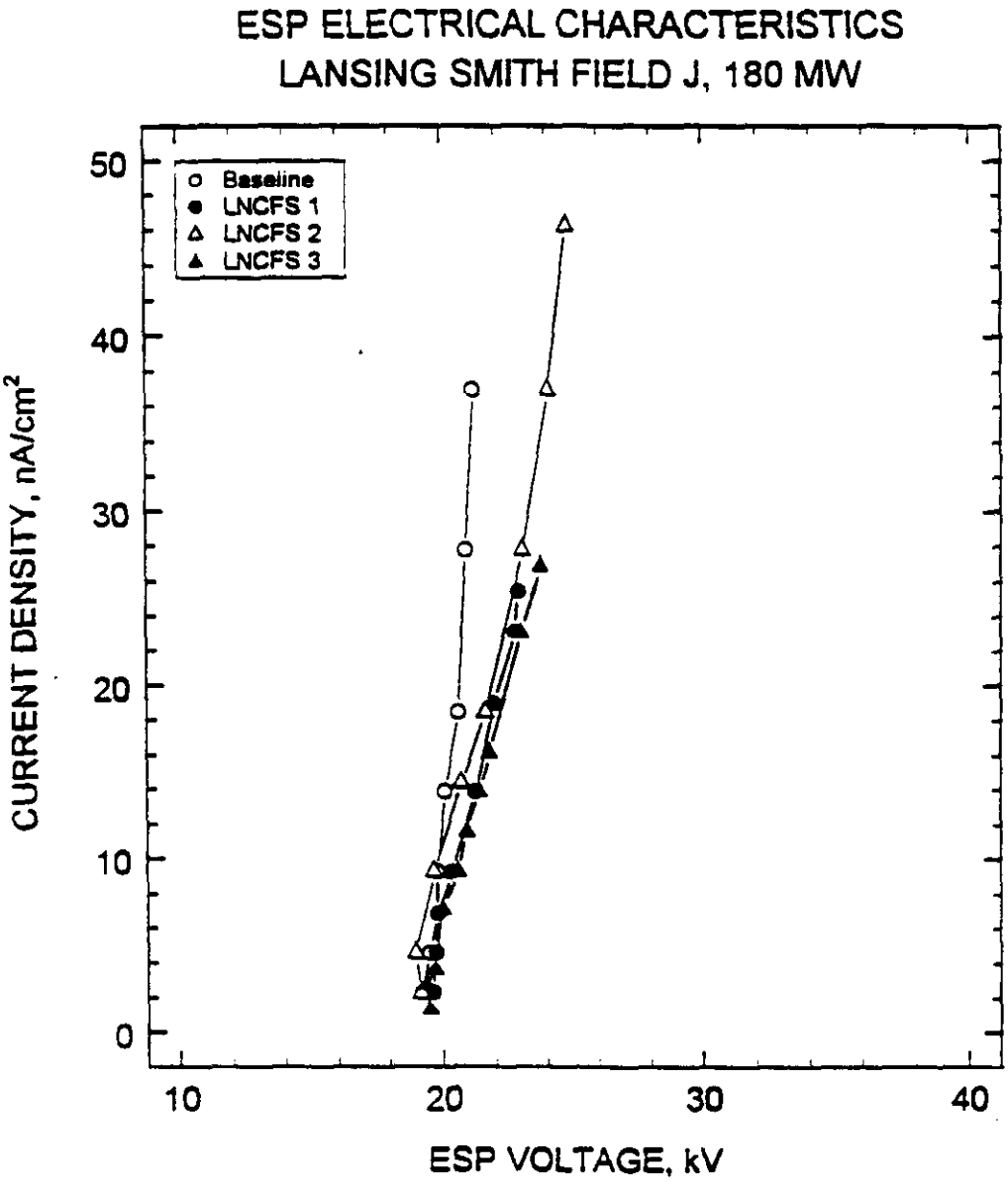

Figure 25. Fourth Field ESP Electrical Characteristics from All Test Phases.

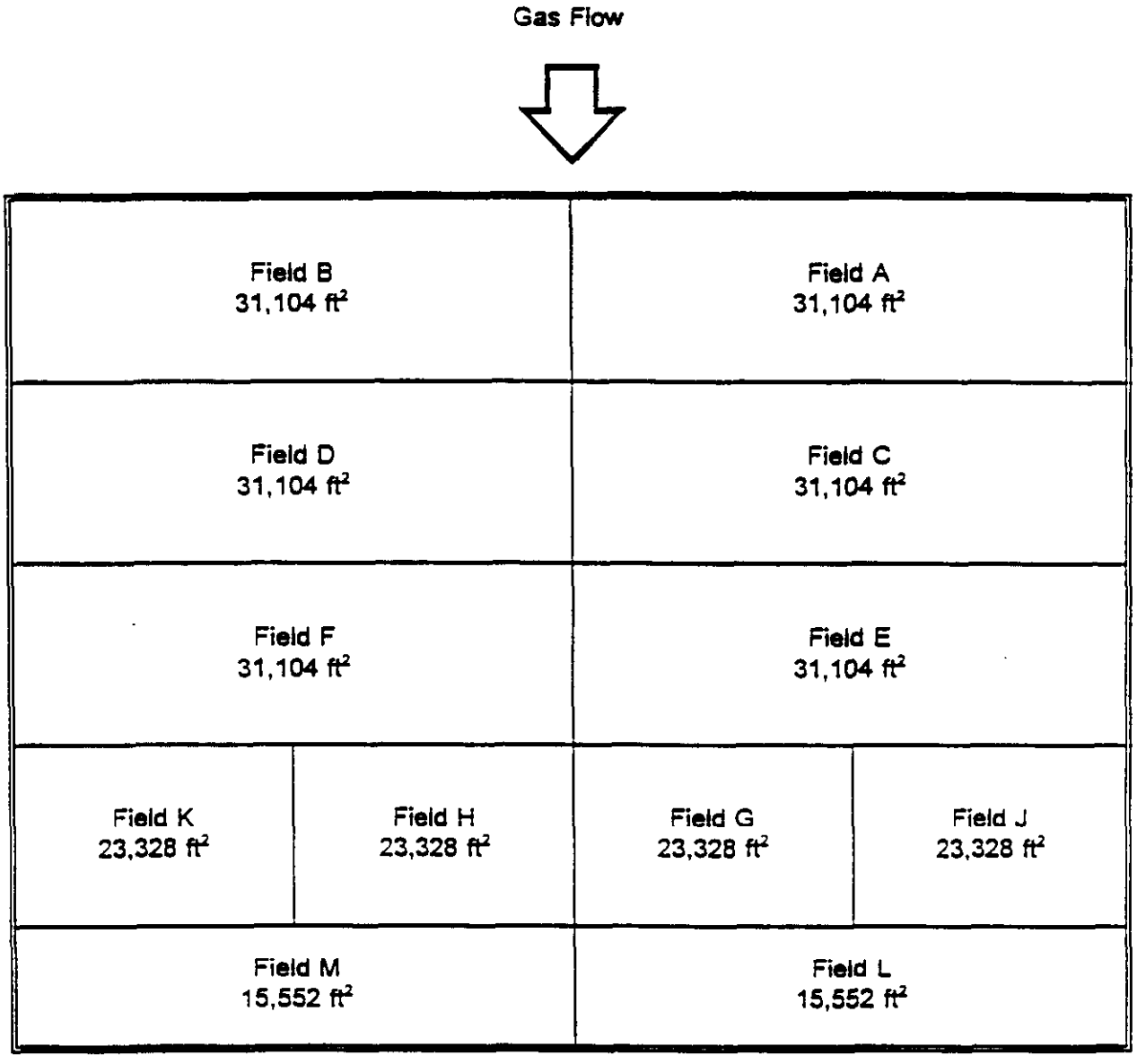

Figure 26. Lansing Smith Unit 2 ESP Configuration.

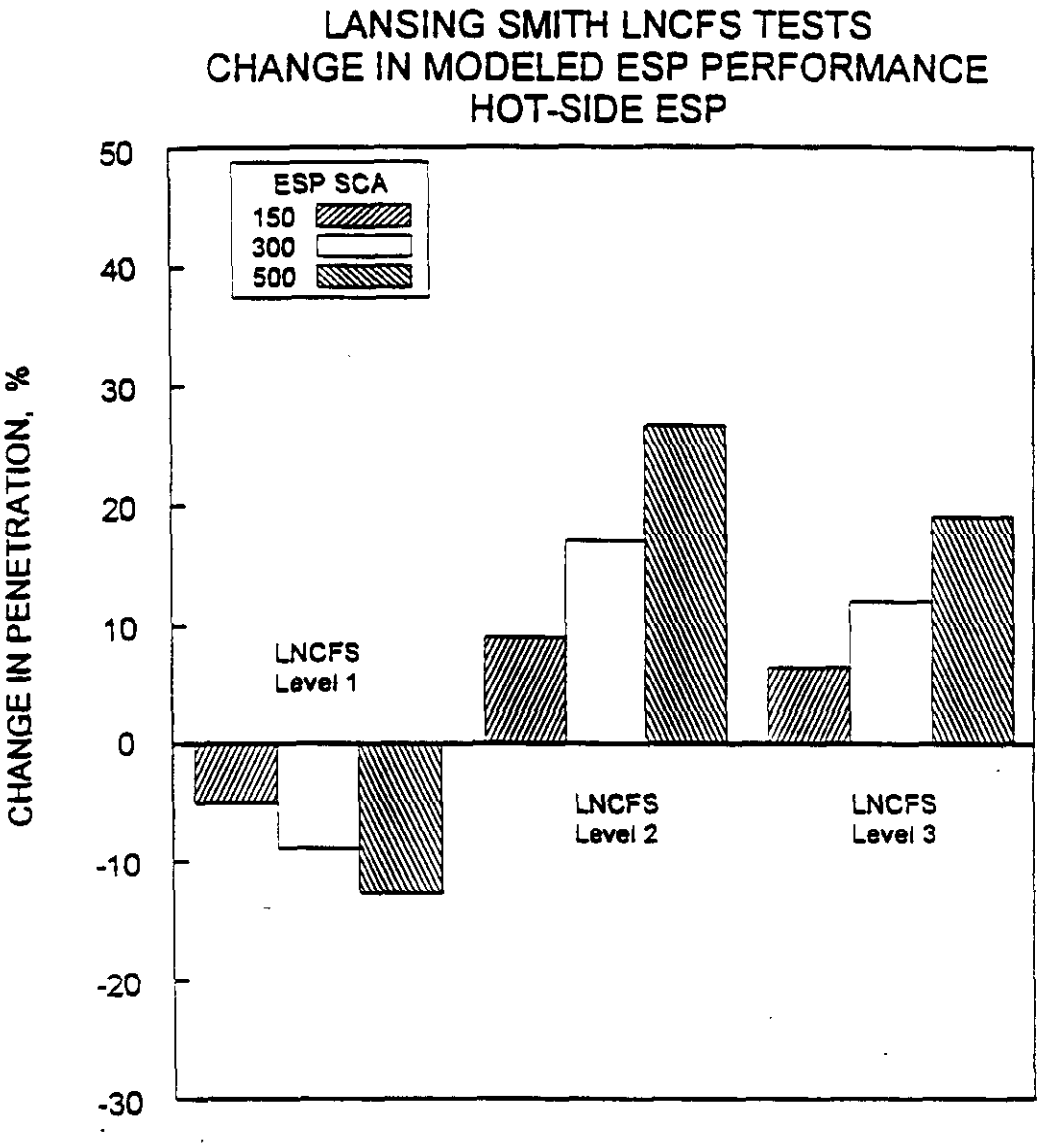

Figure 27. Model Predicted Change in Hot-Side ESP Penetration Because of Changes in Excess Air.

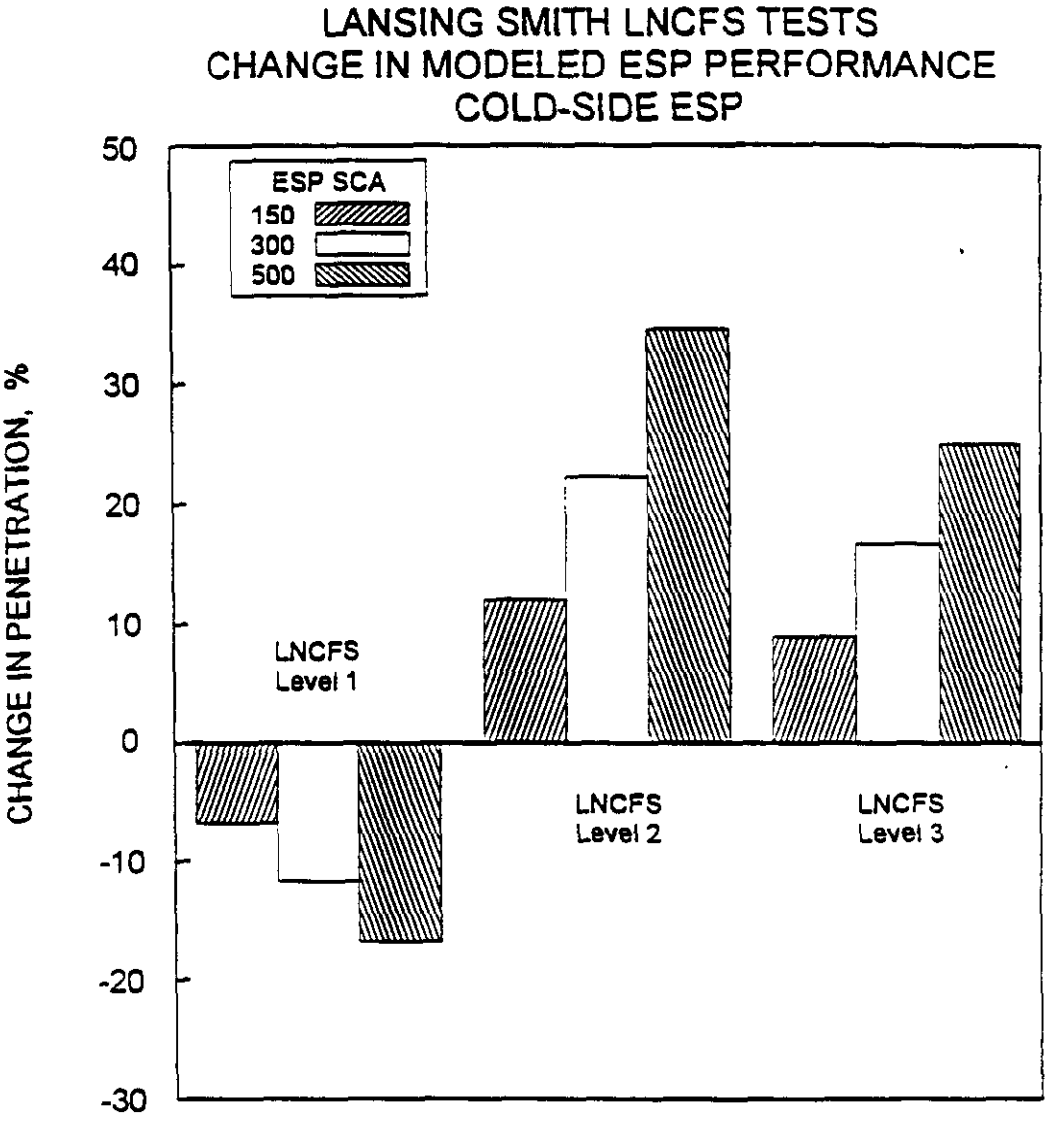

Figure 28. Model Predicted Change in Cold-Side ESP Penetration Because of Changes in Excess Air.

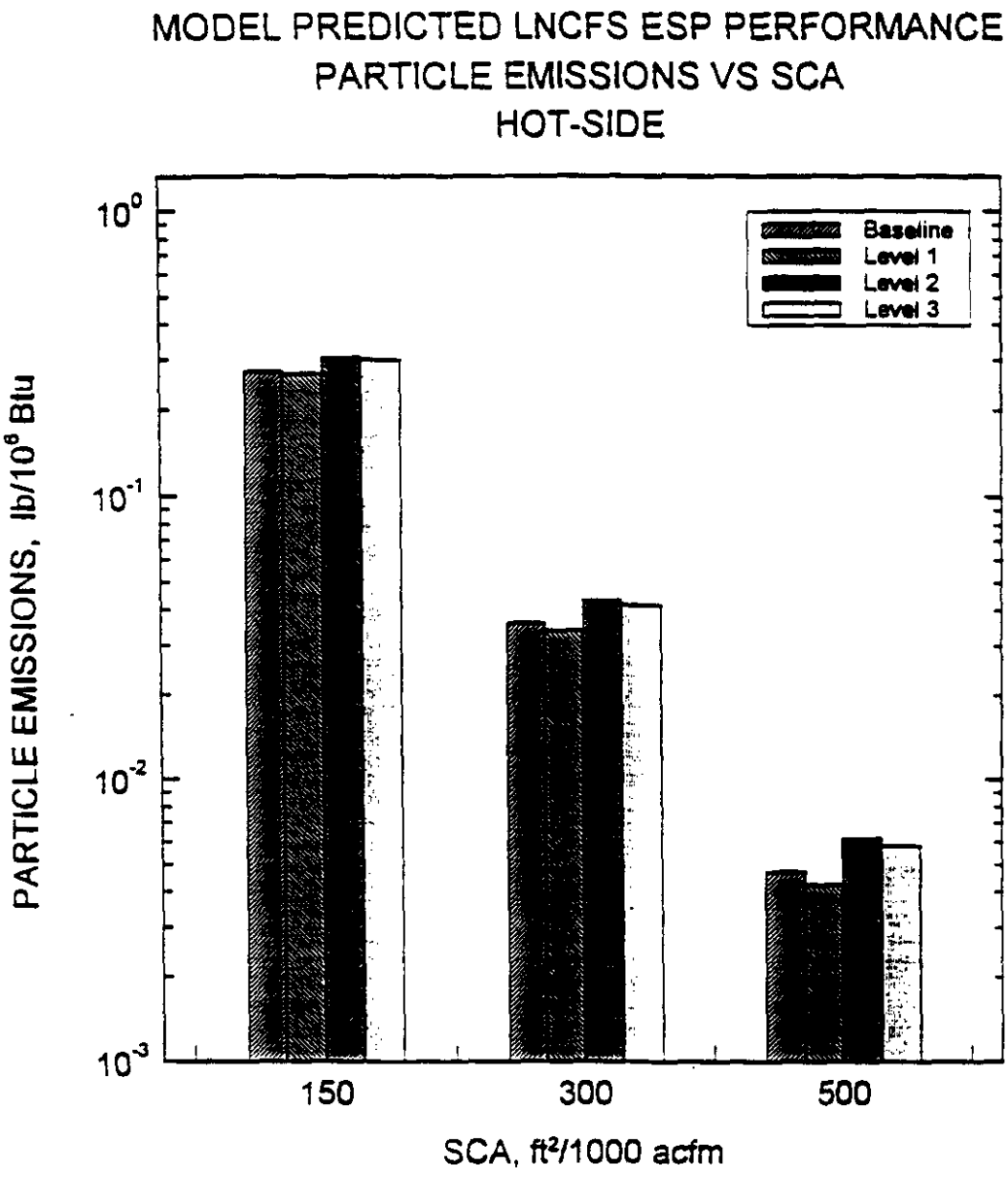

Figure 29. Model Predicted Hot-Side ESP Particle Emissions for All Phases.

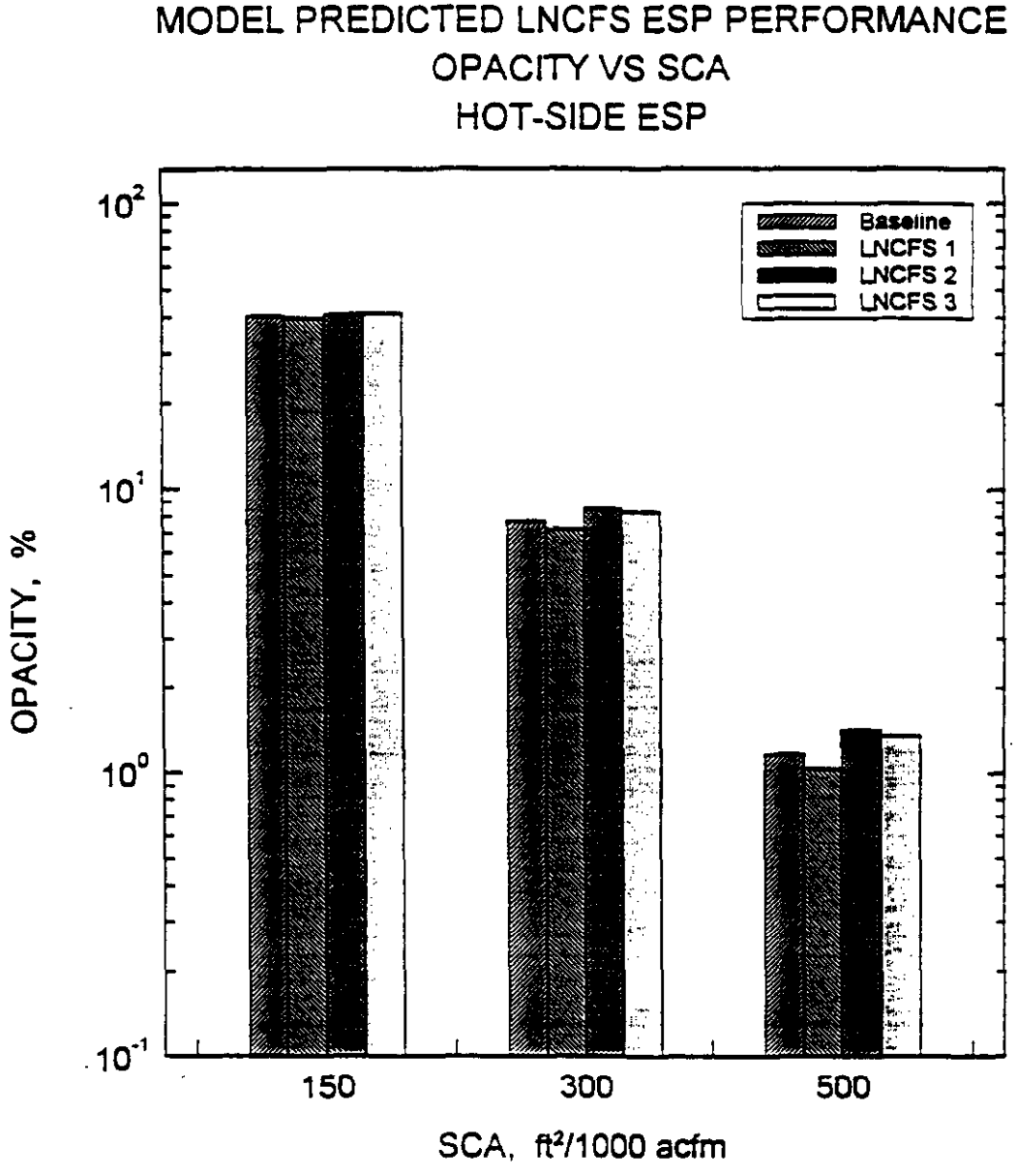

Figure 30. Model Predicted Hot-Side ESP Stack Opacity for All Phases.

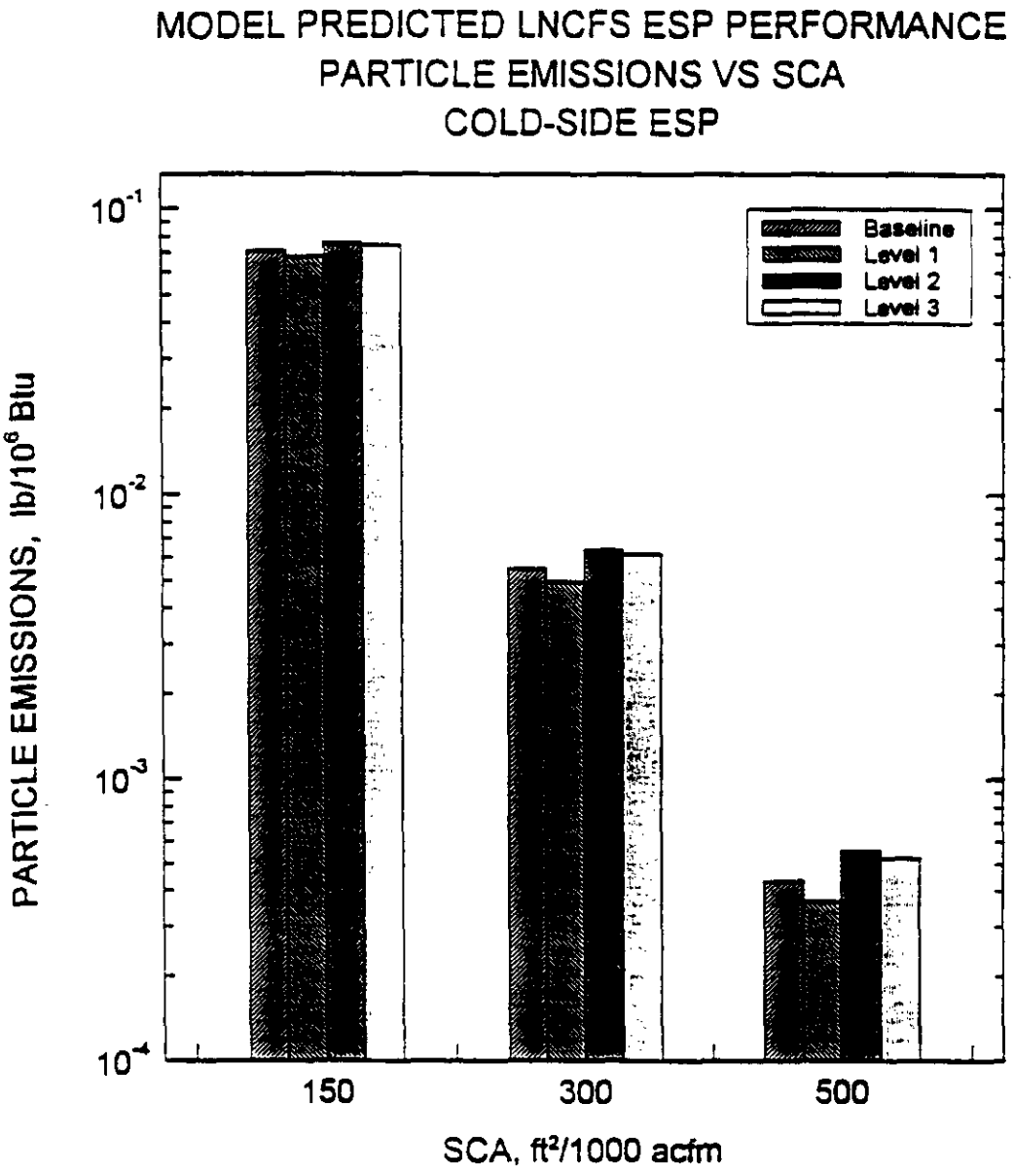

Figure 31. Model Predicted Cold-Side ESP Particle Emissions for All Phases.

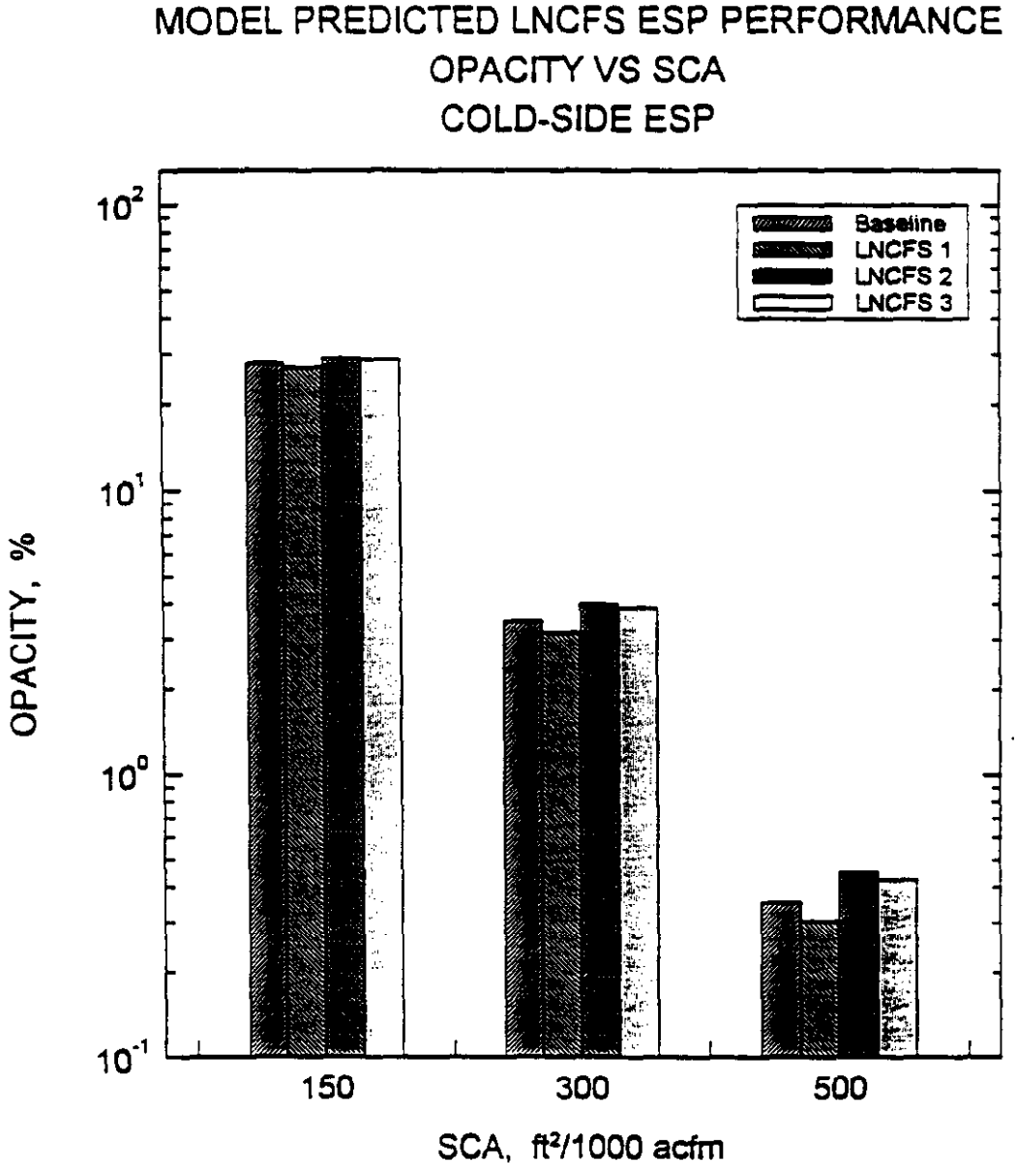

Figure 32. Model Predicted Cold-Side ESP Stack Opacity for All Phases.

Table 1. Effect of LNCFS Modifications on Mass Loading and Gas Flow

Load, MW	Test Condition	Mass Loading			Gas Volume Flow			Gas Temp, °F	Water Vapor, %	Oxygen, %
		gr/acf	gr/dscf	lb/10^6Btu	acfm	dscfm	dscfm at 0% O_2			
200	LNCFS, Level 1	1.18	2.88	4.87	922000	377000	306700	682	10.3	3.5
	LNCFS, Level 2	1.02	2.49	4.45	1066600	435000	341300	698	9.1	4.5
	LNCFS, Level 3	1.34	3.10	5.32	858500	370600	303200	680	7.6	3.8
180	Baseline	1.17	2.69	5.03	901300	390600	293400	665	7.3	5.2
	LNCFS, Level 1	1.09	2.64	4.55	838000	346000	281400	666	10.3	3.9
	LNCFS, Level 2	1.09	2.61	4.93	950400	395200	295000	677	9.6	5.3
	LNCFS, Level 3	1.20	2.80	5.04	896700	385500	298800	667	8.0	4.7
	LNCFS, Level 3[a]	1.24	2.85	5.10	789700	345200	270900	668	7.4	4.5
	LNCFS, Level 3[b]	1.30	3.10	5.54	892000	373000	294500	670	9.3	4.4
135	Baseline	1.25	2.70	4.54	532000	247000	205600	591	8.5	3.5
	LNCFS, Level 1	1.43	3.25	6.06	669000	294000	220900	609	10.2	5.2
	LNCFS, Level 2	1.17	2.66	4.79	720400	317400	247500	617	8.9	4.6
	LNCFS, Level 3	1.36	2.91	5.38	568200	264700	201400	602	7.0	5.0
	LNCFS, Level 3[b]	1.41	3.16	6.00	665000	297000	218800	603	9.2	5.5
115	Baseline	1.30	2.77	4.96	465000	218400	171400	568	8.8	4.5
	LNCFS, Level 1	1.31	2.87	5.46	563000	257000	189400	582	8.9	5.5
	LNCFS, Level 2	1.15	2.57	4.73	614500	276400	210300	588	9.9	5.0
	LNCFS, Level 3	1.37	2.94	5.63	552000	257700	188700	572	8.8	5.6

a. Coal mill classifiers adjusted to produce a finer size distribution.
b. Test repeated after coal mill overhaul.

Table 2. Short and Long Term Full-Load Flue Gas Oxygen Levels

Condition	Short Term[a]	Long Term[b]	
	O_2 Content, %	O_2 Content, %	% Change from Baseline
Baseline	5.2	3.7	–
LNCFS Level 1	3.9	3.2	-13
LNCFS Level 2	5.3	4.5	22
LNCFS Level 3	4.7	4.3	16

a. Measured during SRI mass train measurements.
b. Measured by continuous monitor.

TABLE 3. ESP Inlet Particle Mass Values Corrected for Long-Term Oxygen Concentrations.

Boiler Load	Test Condition	Short-Term Values		Long-Term Values	
		Mass Loading, gr/dscf	Oxygen Content, %	Oxygen Content, %	Adjusted Mass Loading, gr/dscf
200	LNCFS 1	2.88	3.5	3.2	2.93
	LNCFS 2	2.49	4.5	4.5	2.49
	LNCFS 3	3.10	3.8	4.3	3.01
180	Baseline	2.69	5.2	3.7	2.95
	LNCFS 1	2.64	3.9	3.2	2.75
	LNCFS 2	2.61	5.3	4.5	2.74
	LNCFS 3	2.80	4.7	4.3	2.87
	LNCFS 3[a]	2.85	4.5	4.3	2.88
	LNCFS 3[b]	3.10	4.4	4.3	3.12
135	Baseline	2.70	3.5	3.7	2.67
	LNCFS 1	3.25	5.2	3.2	3.66
	LNCFS 2	2.66	4.6	4.5	2.68
	LNCFS 3	2.91	5.0	4.3	3.04
	LNCFS 3[b]	3.16	5.5	4.3	3.41
115	Baseline	2.77	4.5	3.7	2.91
	LNCFS 1	2.87	5.5	3.2	3.30
	LNCFS 2	2.57	5.0	4.5	2.65
	LNCFS 3	2.94	5.6	4.3	3.19

a. Coal mill classifiers adjusted for finer size distribution.
b. After coal mill overhaul.

TABLE 4. Particle Mass Loading Estimated from Coal Ash.

Test Condition	Coal Ash Content, %	Mass Loading, gr/dscf
Baseline	8.8	2.64 ± 0.74
LNCFS 1	8.6	2.59 ± 0.72
LNCFS 2	8.9	2.67 ± 0.75
LNCFS 3	8.8	2.64 ± 0.74

Table 5. Comparison of Ash Compositions from Baseline and LNCFS Tests

Load, MW	Test Condition	Ash Composition, weight %											
		Li_2O	Na_2O	K_2O	MgO	CaO	Fe_2O_3	Al_2O_3	SiO_2	TiO_2	P_2O_5	SO_3	LOI
200	LNCFS, Level 1	0.02	0.73	2.6	0.92	4.4	18.0	19.9	50.4	1.2	0.18	0.80	9.2
	LNCFS, Level 2	0.02	0.56	1.8	0.87	8.5	18.7	18.5	48.5	1.2	0.20	0.83	7.5
	LNCFS, Level 3	0.02	0.70	2.5	0.87	4.9	17.6	19.3	50.8	1.0	0.18	1.20	7.2
180	Baseline	0.02	0.71	2.6	0.96	6.6	18.0	19.0	49.7	1.2	0.23	0.97	7.3
	LNCFS, Level 1	0.02	0.75	2.6	0.91	4.5	18.3	19.6	50.0	1.2	0.18	0.55	6.4
	LNCFS, Level 2	0.02	0.63	1.9	0.90	7.5	18.6	18.6	49.1	1.2	0.21	0.92	7.0
	LNCFS, Level 3	0.02	0.62	2.5	0.91	4.7	17.9	19.5	51.0	1.0	0.19	1.20	6.2
135	Baseline	0.02	0.66	2.7	1.00	5.4	16.2	20.7	51.0	1.2	0.22	1.10	5.2
	LNCFS, Level 1	0.02	0.73	2.6	0.94	4.4	17.3	19.8	50.7	1.2	0.18	0.65	6.7
	LNCFS, Level 2	0.02	0.58	2.2	0.91	7.7	17.5	18.7	49.6	1.2	0.24	0.74	6.1
	LNCFS, Level 3	0.02	0.62	2.6	0.87	4.3	16.5	20.1	51.8	1.1	0.20	0.80	6.2
115	Baseline	0.02	0.60	2.5	0.96	5.5	18.6	20.3	49.5	1.1	0.23	0.88	5.9
	LNCFS, Level 1	0.02	0.80	2.7	0.95	4.2	17.0	19.7	50.8	1.2	0.20	0.60	4.8
	LNCFS, Level 2	0.02	0.63	1.9	0.89	7.5	17.3	18.9	50.1	1.2	0.18	0.75	3.9
	LNCFS, Level 3	0.02	0.70	2.6	0.91	4.3	16.8	20.2	52.0	1.1	0.20	0.98	8.7

Table 6. Effect of LNCFS on Ash Carbon Content and LOI

Load, MW	Test Condition	Mass Train Sample			Hopper Sample LOI, %
		Carbon, %		Total LOI, %	
		>200 Mesh[c]	Total		
200	LNCFS 1	24.8	6.5	6.9	9.2
	LNCFS 2	39.0[c]	4.8	5.4	7.5
	LNCFS 3	24.2	6.3	6.6	7.2
180	Baseline	27.9	4.8	5.0	7.3
	Base - Low O_2	29.1	8.3	8.7	10.5
	LNCFS 1	16.9	4.2	4.6	6.4
	LNCFS 2	39.9[c]	3.8	4.2	7.0
	LNCFS 3	20.9	5.2	5.6	6.2
	LNCFS 3[a]	23.2	5.9	6.1	NA
	LNCFS 3[b]	24.1	6.7	7.0	NA
135	Baseline	18.6	3.6	4.2	5.2
	LNCFS 1	18.0	4.8	5.3	6.7
	LNCFS 2	39.5[c]	3.3	3.9	6.1
	LNCFS 3	23.3	5.6	5.8	6.2
	LNCFS 3[b]	30.9	8.3	8.9	NA
115	Baseline	20.0	3.8	4.0	5.9
	LNCFS 1	16.1	3.8	4.0	4.8
	LNCFS 2	38.6[c]	3.4	3.8	3.9
	LNCFS 3	27.0	6.2	6.6	8.7

a. Coal mill classifiers adjusted for finer size distribution.
b. Test repeated after coal mill overhaul.
c. LNCFS 2 samples sieved with 100 mesh rather than 200 mesh screen.

Table 7. Effect of LNCFS on SO_3 Concentration and SO_3-To-SO_2 Ratio

Boiler Load, MW	Test Condition	Gas Temperature, °F	Concentration, ppm		Percentage of SO_3-to-SO_2
			SO_3	SO_2	
200	LNCFS 1	351	12[c]	2348	0.64
	LNCFS 2	357	13[c]	2306	0.69
	LNCFS 3	324	13[c]	2160	0.74
180	Baseline	333	13[c]	2082	0.62
	Base - low O_2	321	10	2239	0.45
	LNCFS 1	333	12	2346	0.51
	LNCFS 2	332	11	2282	0.48
	LNCFS 3	311	12	2063	0.58
	LNCFS 3[a]	316	13[c]	2160	0.60
	LNCFS 3[b]	342	15	2257	0.66
135	Baseline	296	8	2209	0.36
	LNCFS 1	300	9	2135	0.42
	LNCFS 2	311	7	2232	0.31
	LNCFS 3	281	9	1987	0.45
	LNCFS 3[b]	307	12	2118	0.57
115	Baseline	288	9	2109	0.43
	LNCFS 1	293	9	2077	0.43
	LNCFS 2	295	6	2134	0.28
	LNCFS 3	266	7	1911	0.37

a. Coal mill classifiers adjusted for finer size distribution.
b. Test repeated after coal mill overhaul.
c. Measurements on south duct only - value adjusted for comparison with both sides.

Table 8. Comparison of Hot-Side Resistivities for all Test Phases

Load, MW	Condition	Temp-erature, °F	Resistivity, ohm-cm		
			Laboratory Measurement	Inherent Prediction	Sodium Depleted Prediction
180	Baseline,	665	$1x10^{9}$	$2x10^{9}$	$8x10^{9}$
	LNCFS 1	666	$1x10^{9}$	$9x10^{8}$	$5x10^{9}$
	LNCFS 2	677	$4x10^{9}$	$2x10^{9}$	$8x10^{9}$
	LNCFS 3	667	$1x10^{9}$	$2x10^{9}$	$1x10^{10}$
135	Baseline	591	$5x10^{9}$	$5x10^{9}$	$3x10^{10}$
	LNCFS 1	605	$5x10^{9}$	$3x10^{9}$	$1x10^{10}$
	LNCFS 2	617	$9x10^{9}$	$6x10^{9}$	$3x10^{10}$
	LNCFS 3	602	$7x10^{9}$	$4x10^{9}$	$3x10^{10}$
115	Baseline	568	$7x10^{9}$	$8x10^{9}$	$4x10^{10}$
	LNCFS 1	582	$7x10^{9}$	$3x10^{9}$	$2x10^{10}$
	LNCFS 2	588	$1x10^{10}$	$7x10^{9}$	$4x10^{10}$
	LNCFS 3	572	$1x10^{10}$	$5x10^{9}$	$4x10^{10}$

Table 9. Comparison of Cold-Side Resistivities for all Test Phases (300°F)

Load, MW	Test Condition	Lab Measured Resistivity		Model Predicted Resistivity			
				Measured SO_3		Constant SO_3	
		SO_3, ppm	Resistivity, ohm-cm	SO_3, ppm	Resistivity, ohm-cm	SO_3, ppm	Resistivity, ohm-cm
200	LNCFS 1	4.5	$3x10^8$	15	$2x10^8$	4	$4x10^9$
	LNCFS 2	5.0	$1x10^9$	16	$4x10^8$	4	$6x10^9$
	LNCFS 3	5.0	$3x10^8$	16	$2x10^8$	4	$5x10^9$
180	Baseline	10.0	$2x10^8$	9	$3x10^8$	4	$5x10^9$
	LNCFS 1	4.5	$3x10^8$	12	$4x10^8$	4	$3x10^9$
	LNCFS 2	5.0	$2x10^9$	11	$6x10^8$	4	$5x10^9$
	LNCFS 3	5.0	$4x10^8$	12	$5x10^8$	4	$4x10^9$
135	Baseline	10.0	$1x10^8$	8	$2x10^9$	4	$5x10^9$
	LNCFS 2	5.0	$3x10^9$	7	$2x10^9$	4	$4x10^9$
	LNCFS 3	5.0	$5x10^8$	9	$1x10^9$	4	$6x10^9$
	LNCFS 1	4.5	$2x10^9$	9	$4x10^8$	4	$5x10^9$
115	Baseline	10.0	$2x10^8$	9	$9x10^8$	4	$5x10^9$
	LNCFS 2	5.0	$2x10^9$	6	$2x10^9$	4	$3x10^9$
	LNCFS 3	5.0	$9x10^8$	7	$1x10^9$	4	$4x10^9$
	LNCFS 1	4.5	$2x10^9$	9	$5x10^8$	4	$5x10^9$

Table 10. General ESP Parameters Used in Modeling

	Hot Side		Cold Side	
Number of Fields	3	5, 8	3	5, 8
Collecting Plate Height, ft	30	30	30	30
Length of Each Field, ft	5	6.25	5	6.25
Collecting Plate Spacing, in.	9	9	9	9
Number of Gas Passages	135	135	91	91
Overall ESP Width, ft	101	101	68	68
Collection Area per Field, ft^2	40,500	50,625	27,300	34,125
Wire Spacing, in.	7.5	7.5	7.5	7.5
Wires per Gas Passage per Field	8	10	8	10
Total Wire Length per Field, ft	28,350	40,500	21,840	27,300
Wire Diameter, in.	0.1	0.1	0.1	0.1
Gas Temperature, °F	658	658	300	300
Gas Viscosity, kg/m/s	3.18×10^{-5}	3.18×10^{-5}	2.22×10^{-5}	2.22×10^{-5}
Gas Pressure, atm	0.96	0.96	0.96	0.96
Opacity Path Length, ft	20	20	20	20
Peak-to-Average Voltage Ratio	1.2		1.2	
Electrical Breakdown Strength, V/m	1.5×10^6		1.5×10^6	
Particle Density, kg/m	2350		2350	
Dielectric Ratio	100		100	
Ion Mobility, $m^2/V/s$	2.7×10^{-4}		2.7×10^{-4}	
Gas Sneakage Fraction	0.05, 0.10		0.05, 0.10	
Gas Velocity Standard Deviation	0.15, 0.25		0.15, 0.25	
Rapping Dust MMD, μm	6.0		6.0	
Rapping Dust Sigma	2.5		2.5	

Table 11. Estimated Electrical Conditions used in Lansing Smith ESP Modeling

Condition	ESP Field	ESP Voltage, kV	Current Density, nA/cm^2
Hot-Side ESP	1	30.4	25.0
180 MW	2	30.6	50.0
Inherent Resistivity	3	29.0	50.0
	4	27.1	50.0
	5-9	23.7	46.2
Cold-Side ESP	1	41.2	12.5
180 MW	2	40.1	18.5
	3	38.5	20.7
	4	36.7	27.0
	5-9	33.1	28.3

TABLE 12. Condition Specific ESP Model Input Data

	Baseline	LNCFS 1	LNCFS 2	LNCFS 3
Hot-Side Model				
Flue Gas Oxygen, %	3.7	3.2	4.5	4.3
Gas Volume Flow, acfm	816,000	793,000	857,000	845,000
ESP Gas Velocity, ft/sec	4.50	4.37	4.72	4.66
Particle Mass Loading, gr/acf	1.28	1.32	1.22	1.24
Cold-Side Model				
Flue Gas Oxygen, %	3.7	3.2	4.5	4.3
Gas Volume Flow, acfm	554,600	539,000	582,000	575,000
ESP Gas Velocity, ft/sec	4.50	4.37	4.72	4.66
Particle Mass Loading, gr/acf	1.88	1.93	1.79	1.81

Table 13. Effect of Changing Oxygen Level on Model Predicted Full-Load, Hot-Side ESP Performance

LNCFS Level	ESP Model Non-ideal Conditions, s,σ_g	ESP Particle Penetration, %	Change in Predicted Penetration, %	ESP Collection Efficiency, %	Particle Mass Emissions $lb/10^6$ Btu	ESP Outlet Opacity, %
Nominal SCA = 150						
Baseline	0.05,0.15 0.10,0.25	5.33 7.00	– –	94.67 93.00	0.281 0.369	40 46
1	0.05,0.15 0.10,0.25	5.06 6.69	-5 -4	94.94 93.31	0.267 0.353	40 46
2	0.05,0.15 0.10,0.25	5.81 7.53	9 8	94.19 92.47	0.306 0.396	41 47
3	0.05,0.15 0.10,0.25	5.67 7.38	6 5	94.33 92.62	0.300 0.390	41 47
Nominal SCA = 300						
Baseline	0.05,0.15 0.10,0.25	0.704 1.138	– –	99.296 98.862	0.0371 0.0600	8 11
1	0.05,0.15 0.10,0.25	0.641 1.052	-9 -8	99.359 98.948	0.0339 0.0555	7 11
2	0.05,0.15 0.10,0.25	0.824 1.304	17 15	99.176 98.696	0.0434 0.0687	9 12
3	0.05,0.15 0.10,0.25	0.788 1.255	12 10	99.212 98.745	0.0417 0.0664	8 12
Nominal SCA = 500						
Baseline	0.05,0.15 0.10,0.25	0.092 0.188	– –	99.908 99.812	0.0049 0.0099	1 2
1	0.05,0.15 0.10,0.25	0.081 0.168	-13 -11	99.919 99.832	0.0042 0.0088	1 2
2	0.05,0.15 0.10,0.25	0.117 0.230	27 22	99.883 99.770	0.0062 0.0121	1 2
3	0.05,0.15 0.10,0.25	0.110 0.218	19 16	99.890 99.782	0.0058 0.0115	1 2

Table 14. Effect of Changing Oxygen Level on Model Predicted Full-Load, Cold-Side ESP Performance

LNCFS Level	ESP Model Non-Ideal Conditions, s, σ_g	ESP Particle Penetration, %	Change in Predicted Penetration, %	ESP Collection Efficiency, %	Particle Mass Emissions lb/10^6 Btu	ESP Outlet Opacity, %
Nominal SCA = 150						
Baseline	0.05,0.15 0.10,0.25	1.39 2.16	– –	98.61 97.84	0.0708 0.1110	28 34
1	0.05,0.15 0.10,0.25	1.29 2.03	-7 -6	98.71 97.97	0.0677 0.1070	27 33
2	0.05,0.15 0.10,0.25	1.55 2.36	12 9	98.45 97.64	0.0755 0.1150	29 35
3	0.05,0.15 0.10,0.25	1.51 2.31	9 7	98.49 97.69	0.0742 0.1140	29 35
Nominal SCA = 300						
Baseline	0.05,0.15 0.10,0.25	0.107 0.213	– –	99.893 99.787	0.00548 0.01090	3.5 5.7
1	0.05,0.15 0.10,0.25	0.095 0.191	-12 -10	99.905 99.809	0.00496 0.01000	3.2 5.3
2	0.05,0.15 0.10,0.25	0.131 0.251	22 18	99.869 99.749	0.00638 0.01220	4.0 6.3
3	0.05,0.15 0.10,0.25	0.125 0.242	17 14	99.875 99.758	0.00615 0.01190	3.9 6.2
Nominal SCA = 500						
Baseline	0.05,0.15 0.10,0.25	0.0084 0.0216	– –	99.9916 99.9784	0.00043 0.00110	0.4 0.8
1	0.05,0.15 0.10,0.25	0.0070 0.0185	-17 -14	99.9930 99.9815	0.00037 0.00097	0.3 0.7
2	0.05,0.15 0.10,0.25	0.0114 0.0278	35 29	99.9886 99.9722	0.00055 0.00135	0.5 0.9
3	0.05,0.15 0.10,0.25	0.0106 0.0262	25 21	99.9894 99.9738	0.00052 0.00129	0.4 0.9